Machine Learning Assisted Chemical Characterization and Optical Properties of Atmospheric Brown Carbon in Nanjing, China

Yu Huang[1], Xingru Li[2], Dan Dan Huang[3], Ruoyuan Lei[1], Binhuang Zhou[1], Yunjiang Zhang[1], Xinlei Ge[1, 4*]

[1] Jiangsu Key Laboratory of Atmospheric Environment Monitoring and Pollution Control, Collaborative Innovation Center of Atmospheric Environment and Equipment Technology, School of Environmental Science and Engineering, Nanjing University of Information Science and Technology, Nanjing 210044, China

[2] Analytical Instrumentation Center, Department of Chemistry, Capital Normal University, Beijing, 100048, China

[3] Shanghai Academy of Environmental Sciences, Shanghai 200233, China

[4] School of Environment and Energy Engineering, Anhui Jianzhu University, Hefei 230601, China

*Corresponding author: Xinlei Ge (Email: caxinra@163.com)

For *Atmospheric Chemistry and Physics*

Abstract: The light-absorbing organics, namely brown carbon (BrC), can significantly affect atmospheric visibility and radiative forcing, yet current knowledge of chemical composition of BrC is largely limited to a number of certain classes of compounds; the chemical and optical properties, and particularly linkage between the two remain poorly understood. To address this, a comprehensive analysis was conducted on the particulate matter ($PM_{2.5}$) samples collected in Nanjing, China during 2022 ~ 2023 with a focus on the identification of key BrC molecules. Several important clues related to BrC were found. First, the water-soluble organic aerosol (WSOA) was more oxygenated during cold season (CS) due to a highly oxidized secondary OA (SOA) factor that was strongly associated with aqueous/heterogeneous reactions especially during nighttime, while the WSOA during summer season (SS) was less oxygenated and the SOA was mainly from photochemical reactions. Fossil fuel combustion hydrocarbon-like OA was the largest and dominant contributor to the light absorption during CS (55.6 ~ 63.7%). Secondly, our observations reveals that aqueous oxidation can lead to notable photo-enhancement during CS, while photochemical oxidation on the contrary caused photo-bleaching during SS; Both water-soluble and methanol-soluble organics had four key fluorophores, including three factors relevant with humic-like substances (HULIS) and one protein-like component. Thirdly, molecular characterization show that CHON compounds were overall the most abundant species, followed by CHO and CHN compounds, and significant presence of organosulfates in CS samples reaffirmed the importance of aqueous-phase formation. Finally, building upon the molecular characterization and light absorption measurement results, the machine learning approach was applied to identify the key BrC molecules, and 31 compounds including polycyclic aromatic hydrocarbons (PAHs), oxyheterocyclic PAHs, quinones, and nitrogen-containing species, etc., which can be a good reference for future studies.

1 Introduction

In ambient air, some organic aerosol (OA) species can absorb light in the near-ultraviolet (UV) and visible spectrum, termed as "brown carbon (BrC)" (Andreae and Gelencsér, 2006; Chen et al., 2020b). The BrC absorption exhibits strong wavelength-dependence that typically the absorption increases as the wavelength decreases (Laskin et al., 2015); it can also contribute to the darkening of ice and snow surfaces, particularly in low-latitude and polar regions (Yan et al., 2018; Brown et al., 2022; Chakrabarty et al., 2023). Thus, BrC can play a crucial role in global climate and air quality (Jo et al., 2016; Feng et al., 2013). Some studies show that the global radiative forcing of BrC ranges from approximately 0.22 to 0.57 W m^{-2}, equivalent to 27 ~ 70 % of that of black carbon (BC) (Lin et al., 2014; Zhang et al., 2017). Xu et al. (2024) used a global climate model to estimate that BrC accounts for 19% and 12% of the total light absorption by carbonaceous aerosols, with the direct radiative forcing of 0.110 W m^{-2} and 0.205 W m^{-2} in China during winter and summer, respectively. Delessio et al. (2024) estimated a top-of-the-atmosphere (TOA) radiative effect of BrC to be 0.04 W m^{-2}.

The sources of atmospheric BrC are highly complex, as it can originate from multiple primary sources (Hecobian et al., 2010; Chakrabarty et al., 2010; Gu et al., 2022) as well as various secondary chemical processes (Fleming et al., 2020; Jiang et al., 2021; Chen et al., 2020b; Wang et al., 2021). The primary sources mainly include coal combustion, biomass burning, and vehicular emissions (Wang et al., 2016; Sun et al., 2016; Qi et al., 2019; Chen et al., 2018; Gu et al., 2022); besides, a significant presence of chromophores originating from the ocean has been observed, indicating that the ocean/marine emission is likely also an important source of BrC (Cavalli et al., 2004). As said, secondary BrC species can be generated from many processes, for instances, the aromatic secondary OA (SOA) species formed under high NO_x concentrations (Liu et al., 2024), reaction products of biogenic or anthropogenic SOAs with nitrogen-containing substances such as NH_3 and NH_4^+ (Updyke et al., 2012; Shapiro et al., 2009; Bones et al., 2010), and aqueous-phase reaction products from various carbonyl/phenolic precursors in cloud, fog, and aerosol water (Hu et al., 2017;

Wang et al., 2021; Li et al., 2023; Ou et al., 2021).

The optical properties of BrC are closely related with sources and composition of OA. Recent studies have linked BrC light absorption with various sources resolved from factor analysis of OA determined by the aerosol mass spectrometry (AMS) (Chen et al., 2020b; Zhong et al., 2023; Chen et al., 2016), and provided the mass absorption efficiency (MAE) of individual BrC source/factor. Current studies have identified several classes of light-absorbing organics in ambient OA, such as aromatic carboxylic acids, phenols, nitroaromatic compounds (NACs), polycyclic aromatic hydrocarbons (PAHs) and their derivatives (Lin et al., 2018; Huang et al., 2018; Wang et al., 2021; Xing et al., 2023; Gu et al., 2022; Chen et al., 2020b; Kuang et al., 2023; Laskin et al., 2025). Some lignin pyrolysis/burning products including coumarins, flavonoids, stilbenes, and several sulfur-containing species are also significant BrC constituents (Fleming et al., 2020; Budisulistiorini et al., 2017; Huang et al., 2022). Xing et al. (2023) identified a series of BrC chromophores, encompassing nitrophenols, benzoic acids, oxygenated PAHs, phenols, aryl amides/amines, phenylpropene derivatives, coumarins and flavonoids, pyridines, and nitrobenzoic acids. Nevertheless, knowledge regarding the molecular composition of BrC so far is still incomplete and the identified species only occupy a limited fraction of the BrC total light absorption (<25%) (Wang et al., 2024). For examples, Zhang et al. (2013) measured eight NACs in Los Angeles and found that they contributed about 4 % of water-soluble BrC light absorption at 365 nm; Huang et al. (2018) measured 18 PAHs and their derivatives in Xi'an and found that they accounted for on average ~ 1.7 % of the overall absorption of methanol-soluble BrC; Gu et al. (2022) quantified eight NACs present in $PM_{2.5}$ during winter in Nanjing, which together accounted for at most ~9 % of the total BrC absorption at 365 nm. On the other hand, the fluorescent properties of OA can be determined by the excitation-emission matrix (EEM) fluorescence spectroscopy (Murphy et al., 2013; Stubbins et al., 2014). By performing the parallel factor analysis (PARAFAC) on EEM data, the key fluorophores can be identified (Xie et al., 2020; Chen et al., 2020a; Chen et al., 2021). These fluorophores are also linked with different sources such as biomass burning, coal

combustion, and vehicle emissions (Tang et al., 2020).

Emerging non-targeted approaches based on gas chromatography (GC) or liquid chromatography (LC) coupled with high-resolution mass spectrometry can detect hundreds to thousands of molecules in OA (Kuang et al., 2023; Mao et al., 2022), enabling the identification of potential BrC species by connecting them with light absorption of OA. However, these approaches often output multi-dimensional data with numerous variables, which must be evaluated appropriately. Traditional statistical methods often perform poorly when handling large datasets and fail to accurately elucidate complex interplays among variables (Fasola et al., 2020). Machine learning (ML) is a powerful tool to effectively resolve such nonlinear relationships and address issues of collinearity among variables (Tang et al., 2024). For instances, Zhang et al. (2023) employed the Random Forest (RF) algorithm to quantify the factors driving $PM_{2.5}$ trends in Tibetan Plateau from 2015 to 2022, revealing the importance of anthropogenic emission reductions, and a similar ML approach was used for resolving the driving factors of ozone pollution too (Zhu et al., 2024). Li et al. (2022b) applied the ML-RF approach to analyze the sources of OA in submicron PM (PM_1) and $PM_{2.5}$, showing the importance of secondary processes in supermicron PM. Wang et al. (2022a) integrated the positive matrix factorization (PMF) with a multi-layer perceptron (MLP) neural network to analyze the sources of BrC light absorption. Very recently, Wang et al. (2024) applied the ML method to predict the optical properties of BrC with known chromophores.

In this study, we conducted a systematic investigation on the chemical and optical properties on the fine particular matter ($PM_{2.5}$) samples in both daytime and nighttime collected in Nanjing, China during summer and cold seasons of 2022 ~ 2023. Particularly, for the first time, we applied the ML-RF algorithm to connect the light-absorbing characteristics with the determined organic molecules, aiming to identify more unknown key BrC molecules. Our findings regarding the BrC properties, especially the BrC molecules identified can be a good reference, and the ML application can be an example of practice for future studies as well.

2 Experimental methods

2.1 Sampling site and sample collection

The $PM_{2.5}$ filter samples were collected in Nanjing, China, from July 11 to August 23, 2022, November 30 to December 10, 2022, February 13 to February 20, 2023, and March 3 to March 31, 2023. The first period represents the hot summer season (SS) (81 samples), and the later three periods represent the cold season (CS)(83 samples); note samples were not collected during precipitation in both seasons. The sampling site was located inside the campus of Nanjing University of Information Science and Technology (32°12'20.82"N, 118°42'25.46"E). The site was in a suburban area, surrounded by residential buildings, close to traffic arteries, and industrial zones (including chemical engineering, petrochemical, power plants and ironmaking and steelmaking plants).

A high volume sampler (Jinshida Ltd. Qingdao, China, model KB-1000) with a flow rate of 1.05 m^3 min^{-1} was employed. $PM_{2.5}$ samples were collected on the prebaked (450 ºC) quartz fiber filters (Pallflex, USA, size of 8 × 10 inch). Daytime samples were collected from 08:00 to 18:00 (Local Beijing time), and nighttime samples were collected from 19:00 to 07:00 on the next day. Each filter was wrapped in an aluminum foil and kept frozen at -20 °C until analysis. The concentrations of common gas pollutants (SO_2, NO_2, CO, and O_3) were obtained from the nearby National Environmental Monitoring Center (http://www.cnemc.cn/), while the meteorological parameters (air temperature, relative humidity, wind speed and direction) were recorded in the same site as $PM_{2.5}$.

2.2 Chemical analyses

2.2.1 Measurements of inorganic ions, organic carbon (OC) and elemental carbon (EC)

A number of round pieces (20 mm diameter) were punched from each sample filter, and were extracted by using 50 mL of ultrapure water (18.25 MΩ cm) (10 pieces) and

methanol (4 pieces), respectively. The filter pieces underwent 30 minutes of sonication and were filtrated through the polytetrafluoroethylene (PTFE) syringe filters (0.22 μm) to remove insoluble materials. Cations (NH_4^+, Na^+, K^+, Mg^{2+}, Ca^{2+}) were measured using a 881 Compact IC Pro (Metrohm, Switzerland), anions (NO_3^-, SO_4^{2-}, Cl^-, F^-) were determined by the ICS2100 (Dionex, USA). The water-soluble organic carbon (WSOC) (μg C m^{-3}) was measured by a total organic carbon (TOC) analyzer (TOC-L, Shimazu, Japan). Operational details of these analyses can be found in our previous work (Chen et al., 2020a).

Concentrations of total elemental carbon (EC) and organic carbon (OC) in samples were measured using a thermal optical carbon analyzer (RT-4; Sunset Laboratory, USA) on a separate round filter piece (17 mm diameter) by using the IMPROVE TOT protocol (Bai et al., 2020). In addition, the residual OC and EC contents in samples after methanol extraction were determined with the same method above, and were subtracted from the total OC content, to derive the methanol-soluble OC (MSOC) (μg C m^{-3}).

2.2.2 Bulk analysis of organics

We employed specially an Aerodyne soot particle AMS (SP-AMS) to determine the bulk composition of water-soluble OA (WSOA) (Onasch et al., 2012). It should be noted that, direct AMS analysis on the methanol-soluble OA (MSOA) is currently unfeasible, even though it might be more important than WSOA in both concentration and light absorption. Likewise almost all offline AMS analysis methods (O'brien et al., 2019; Vasilakopoulou et al., 2023), this is due to that the methanol solvent and its associated organic impurities cannot be effectively removed, making the obtained MSOA signals unidentifiable.

The analysis procedure of WSOA is similar to that described in Ge et al. (2017). In brief, eight round pieces (20 mm diameter) of each filter were sonicated in 40 mL of ultrapure water, and the aqueous extract was nebulized using an atomizer (TSI, Model 3076), then the mist was dried by a silica gel diffusion dryer and the remaining particles were sent to the SP-AMS. The SP-AMS was operated in a laser-off mode, therefore it measured non-refractory species that can be rapidly vaporized at 600 °C (SP-AMS oven

temperature). Note the SP-AMS employs a 70 eV electron impact (EI) ionization scheme, so the vaporized species are fragmented into positively charged ions with different mass-to-charge (*m/z*) ratios and we obtained the composition of WSOA in the form of lumped molecular fragments rather than detailed molecular composition.

The SP-AMS data were post-processed using the Igor-based ToF-AMS analysis toolkit (SQUIRREL version 1.56D and PIKA version 1.15D). Elemental ratios including hydrogen-to-carbon (H/C), oxygen-to-carbon (O/C) and nitrogen-to-carbon (N/C) as well as the organic mass to organic carbon (OM/OC) ratio were calculated by using the methods proposed in Aiken et al. (2008), Canagaratna et al. (2015) and Ge et al. (2024). The WSOA mass concentration of each sample was normalized by multiplying the WSOC concentration with its corresponding OM/OC. Then, we conducted the PMF analysis to resolve the sources of WSOA by utilizing the PMF evaluation toolkit (Version 2.06) (Ulbrich et al., 2009), followed strictly the protocol described in Zhang et al. (2011). As usual, we included only ions with $m/z \leq 120$, and PMF solutions were explored by varying the number of factors (from 3 to 8) and rotation parameters (f_{peak}, from -1 to 1 with an increment of 0.2). Based on the diagnostic plots in Fig. S1 in the supplement, the four-factor solution was selected as the best solution. The factors include a hydrocarbon-like OA (HOA) relevant with fossil fuel combustion, a biomass burning-related OA (BBOA), a less oxidized oxygenated OA (OOA1) and a more oxidized oxygenated OA (OOA2) (see details in Sect. 3.1.2).

2.2.3 Molecular characterization of organics

Molecular-level characterization of organic species was conducted by using an ultra-high performance liquid chromatography with a quadrupole time-of-flight (QTOF) mass spectrometer (UPLC-QTOF-MS) (ACQUITY UPLC H-Class coupled with a Xevo G2-XS QTOF, Waters). The sample pretreatment was described in Text S1, and the analyzed organics are those dissolved in methanol (namely MSOA). Compound separation was performed with a Luna Omega 1.6 μm C18 column (100 mm × 2.1 mm × 1.6 μm), and the sample aliquot was subjected to electrospray ionization (ESI), and detected in both positive and negative ion modes. The scanning *m/z* range for each mass

spectrum was 50-1200, with a scanning rate of one spectrum per 0.1 second. More details are presented in Text S2.

The original UPLC-QTOF-MS data were processed using the Mass Spectrometry-Data Independent Analysis (MS-DIAL, version 4.92) software (Tsugawa et al., 2015), including peak extraction, alignment and deconvolution, achieving a detection probability of 70% in all samples for any identified compound. The method of systematic error removal using random forest (SERRF, a ML algorithm), was then introduced to reduce systematic errors and normalize the measured data (Fig. S2). All deconvoluted spectra were imported into the SIRIUS (Version 5.6.2) toolkit (Dührkop et al., 2019) to determine molecular formulas. The semi-quantitative concentrations of identified molecules were expressed in the normalized peak areas (NPRs), defined as their peak areas acquired from SERRF divided by air volumes of the samples.

In addition, the double-bond equivalent (DBE) was used to indicate the level of unsaturation of the compound (Bae et al., 2011), and the aromaticity equivalent (Xc) (Yassine et al., 2014) was used to indicate the molecular structure. O/C, H/C and DBE values of the sample were averaged over all identified molecules based on their relative abundances (See details in Text S3).

2.3 Optical analyses

2.3.1 Light absorption properties

The light absorption spectra of both WSOC and MSOC in 200 ~ 800 nm were obtained using a UV-Vis spectrophotometer (UV-3600, Shimadzu, Japan) with a 0.5 nm interval. The absorbance at a certain wavelength λ (A_λ) were corrected by subtracting that at 700 nm (A_{700}) (near zero, as background), and the corresponding light absorption coefficient (Abs_λ, M m^{-1}) is calculated as below (Hecobian et al., 2010):

$$Abs_\lambda = (A_\lambda - A_{700}) \times \frac{V_l}{V_a \times L} \times \ln(10) \quad (1)$$

Where V_l represents volume of the extract (water or methanol), V_a denotes air volume of the filter piece, and L is the optical path length (0.01 meters here).

The corresponding mass absorption efficiency (MAE_λ, m^2 g^{-1}) can then be

calculated below:

$$\mathrm{MAE}_{\lambda} = \frac{\mathrm{Abs}_{\lambda}}{[\mathrm{WSOC}]\ \ ([\mathrm{MSOC}])} \quad (2)$$

Where [WSOC] ([MSOC]) represents the mass concentration of WSOC (MSOC). Following previous studies (Laskin et al., 2015; Chen et al., 2018; Xie et al., 2020; Chen et al., 2020b), the light absorption at 365 nm (Abs_{365}) was employed as a surrogate for BrC in this work.

The relationship between the Absorption Ångström Exponent (AAE)(an index of the wavelength dependence) (Andreae and Gelencsér, 2006) and light absorption is shown below:

$$Abs_{\lambda} = K \cdot \lambda^{-AAE} \quad (3)$$

Where *K* is a constant related to light absorption, and we computed the AAE values in the 300 ~ 450 nm range.

Additionally, a multi-linear regression (MLR) method was used to estimate the contributions of different WSOA factors to the light absorption of total WSOA, as shown in the following equation :

$$\mathrm{Abs}_{365,\mathrm{WSOC}} = a \times \mathrm{HOA} + b \times \mathrm{BBOA} + c \times \mathrm{OOA1} + d \times \mathrm{OOA2} \quad (4)$$

Here, HOA, BBOA, OOA1, and OOA2 represent time series of the WSOA factors. *a*, *b*, *c*, and *d* are the fitting parameters, which are the mass absorption efficiency (MAE) values of corresponding factor.

The direct radiative forcing effect of BrC can be represented by the simple forcing efficiency (SFE) (in W g^{-1}), which is the energy added to the earth-atmosphere system per unit mass of aerosol (Bond and Bergstrom, 2006). The SFE of BrC at the wavelength λ can be expressed below (Chen and Bond, 2010):

$$\frac{\mathrm{dSFE}}{\mathrm{d}\lambda} = -\frac{1}{4}\frac{\mathrm{dS}(\lambda)}{\mathrm{d}\lambda}\tau_{\mathrm{atm}}^{2}(\lambda)(1-F_{\mathrm{C}}) [2 \times (1-\alpha_{\mathrm{S}})^{2}\beta(\lambda)\mathrm{MSE}(\lambda) - 4 \times \alpha_{\mathrm{S}} \times \mathrm{MAE}(\lambda)]\mathrm{d}\lambda \quad (5)$$

Where S(λ) represents the solar irradiance at λ obtained from the ASTM G173–03 reference spectra. τ_{atm} denotes the atmospheric transmission (0.79), F_C is set to 0.6, indicating the fraction of cloud cover, the global average value of α_s is fixed at 0.19, representing the surface albedo, β is the backscatter fraction, and MSE and MAE are

the mass scattering efficiency and mass absorption efficiency of BrC, respectively. .

When estimating the radiative effect of BrC, the direct radiative forcing caused by aerosol scattering can be neglected. Therefore, the absorbed radiative forcing within a given spectral range is calculated by the simplified Eq. (6):

$$\mathrm{SFE} = \int \frac{\mathrm{dS}(\lambda)}{\mathrm{d}_\lambda} \tau_{\mathrm{atm}}^2(\lambda)(1 - \mathrm{F}_C) \times \alpha_{\mathrm{S}} \times \mathrm{MAE}(\lambda)\, \mathrm{d}\lambda \quad (6)$$

2.3.2 Fluorescence properties

Characterization of excitation-emission matrix (EEM) of the extracts was performed using a fluorescence spectrophotometer (Cary Eclipse, Agilent, USA) The wavelength range of excitation was set from 230 to 500 nm, and that of emission was from 250 to 600 nm, the scanning resolutions of excitation and emission were 5 nm and 2 nm, respectively, with the scanning speed of 1200 nm min^{-1}. The photomultiplier tube (PMT) detector voltage was set at 600 V. The measurement was subjected to instrument calibration, internal filter correction, Raman/Rayleigh scattering correction, and all EEM spectra were subjected to blank filter subtraction. The processed data were further analyzed using PARAFAC to group potential components with similar fluorescent properties. The analysis was performed using MATLAB 2022b software with the drEEM toolbox (Murphy et al., 2013).

Fluorescent properties of the extracts were also characterized by the humification index (HIX), biological index (BIX), and fluorescence index (FI). HIX is defined as the ratio of integrated fluorescence emission intensity in the range of 435 - 480 nm to that in the range of 300 to 345 nm when excited at 254 nm; BIX is calculated as the ratio of emission intensity at 380 nm to that of 430 nm for the excitation wavelength of 310 nm; FI is the ratio of emission intensity at 470 nm to that of 520 nm under a fixed 370 nm excitation wavelength (Birdwell and Engel, 2010; Mcknight et al., 2001).

2.4 Machine learning identification of key light-absorbing species

The ML RF model was used here to screen the key light absorbing species by linking the target variable (Abs_{365}) with the identified organic molecules (in NPRs), via the “randomforest()” function in R software (Version 4.3.2). Note since molecular

characterization was conducted on MSOA (not WSOA), therefore light absorption data of MSOA were also used here for consistency. The model included 500 decision trees and estimated the variance through a cross-validation during training. The dataset was divided into a training set (80% of total) and a test set (20% of total) to assure accuracy and robustness of the model.

The model outputted two key indices to assess the importance of each molecule to the light absorption. One metric is IncNPu_val, which can measure the purity of nodes. During the construction of each tree in the RF model, each split can increase the purity of nodes, therefore if more frequently a variable is used in splitting, more contribution it has to the increase of purity of nodes, then the variable is considered to be important. IncMSE_val is another index based on the mean squared error (MSE). When we permute a variable, increase in the projected error can serve as a measure of its importance. If a variable with a significant impact on the predicted results is permuted, the model's MSE would increase significantly, resulting in a high IncMSE_val value (González et al., 2015). Under the 50^{th} percentile of IncMSE_val, some variables had zero or even negative contributions to IncMSE_val. Considering the definition of IncMSE_val, such variables would have either no or negative influence on model fitting, thus only the top 50 % of compounds were chosen. Afterwards, intersection of the two indices were considered as potential BrC chromophores.

Moreover, a molecule typically requires a substantial uninterrupted conjugation on its molecular backbone to effectively absorb visible light (Lin et al., 2018), therefore a compound with the ratio of DBE to carbon (DBE/C) greater than that of linear polyenes (with a molecular formula of C_xH_{x+2}, DBE/C = 0.5) (Cain et al., 2014) is treated as a potential BrC compound. Besides, the DBE/C ratio should be less than the upper limit of DBE for natural compounds (DBE/C = 0.9) (Lobodin et al., 2012). Finally, the candidate compounds passed aforementioned criteria were compared with those in open-source databases, including MoNA (https://mona.fiehnlab.ucdavis.edu/) and MassBankEU (https://massbank.eu/), to be interpreted as the key BrC compounds.

3 Results and discussion

3.1 Chemical properties

3.1.1 General characteristics

During the sampling period, the temperatures were 34.34 ± 3.23 °C (daytime) (± one standard deviation, hereinafter) and 30.85 ± 2.97 °C (nighttime) during SS, 13.00 ± 6.04 °C (daytime) and 9.97 ± 5.04 °C (nighttime) during CS, and the relative humidity (RH) levels were 53.61 ± 10.33 % (daytime) and 65.88 ± 9.87 % (nighttime) during SS, 47.81 ± 18.94 % (daytime) and 55.56 ± 15.74 % (nighttime) during CS, respectively (Figs. 1a and b). Figure 1c depicts the temporal variations of different components. Average concentrations of OC, EC, WSOC, MSOC and total ionic species during daytime and nighttime in the two seasons are summarized in Table 1. Clearly, concentrations of all components were higher in CS than those in SS, but the daytime/nighttime differences were relatively small in both seasons. Also, the MSOC levels were larger than WSOC in all samples. MSOC occupied 82.4 % and 81.5 % while WSOC occupied 61.3 % and 49.5 % of the total OC during SS and CS, respectively, indicating that methanol can more effectively extract the aerosol organics than water.

The mean mass contributions of different ions to their total during SS and CS, respectively are shown in Fig. 1c too. The particles were overall neutral as the molar ratios of inorganic anions to cations were 0.97 and 0.98 during SS and CS, respectively (Fig. S3). The most abundant ion was sulfate in SS (45.5 %) and nitrate in CS (50.7 %), as low temperatures during CS favor the partitioning of nitrate to particle phase. As so, the sulfur oxidation ratio (SOR, $[SO_4^{2-}]/([SO_4^{2-}]+[SO_2])$) and nitrogen oxidation ratio (NOR, $[NO_3^-]/([NO_3^-]+[NO_2])$) were 0.58 and 0.16 (daytime) and 0.56, 0.17 (nighttime) during SS, 0.40, 0.28 (daytime) and 0.42, 0.30 (nighttime) during CS, respectively. NOR was indeed much higher in CS especially during nighttime than those in SS. Furthermore, ammonium (NH_4^+) was the predominant cation while sulfate, nitrate and chloride were major anions. The scatter plots of molar concentrations of ammonium versus summed sulfate, nitrate and chloride (Fig. S4) reveal different bonding forms of the aerosol inorganic salts in different seasons. The correlations were both tight

(correlation coefficients close to 1) yet the fitted slopes during SS were 0.80 (daytime) and 0.89 (nighttime) while those during CS were 0.98 (daytime) and 0.99 (nighttime), respectively. Such results demonstrate that ammonium was deficit to neutralize the cations therefore significant amounts of metal salts (such as sodium/calcium sulfate/nitrate) could exist during SS while during CS, most inorganic species were in the forms of $(NH_4)_2SO_4$, NH_4NO_3 and NH_4Cl with no appreciable metal salts.

3.1.2 Features and sources of water-soluble organics

Regarding the water-soluble portion of organic species (WSOA), Figure 2a presents the average high resolution mass spectra (HRMS) during SS and CS, respectively. It can be seen that, WSOA during CS appeared to be much more oxygenated than that during SS (O/C: 0.58, 0.59 vs. 0.44, 0.45) . To further unravel causes of such differences, PMF analysis were conducted and the HRMS of resolved factors are presented in Fig. 2b, while mass contributions of these factors during SS and CS as well as the Pearson's correlation coefficents (*r*) of these factors with other components are illustrated in Fig. 3.

The HOA MS was dominated by $C_xH_y^+$ ions (57.2 %), such as $C_4H_7^+$ (*m/z* 55) and $C_4H_9^+$ (*m/z* 57), primarily originating from hydrocarbons emitted from fossil fuel combustion (such as traffic) (Canagaratna et al., 2004). Among the four factors, HOA exhibited the lowest O/C ratio (0.24) and the highest H/C ratio (1.66). This is consistent with the behaviors of HOA from a number of previous offline AMS studies (Daellenbach et al., 2017; Liu et al., 2021; Ye et al., 2017; Qiu et al., 2019). The second factor was identified as BBOA, since it has distinct peaks at *m/z* 60 (mainly $C_2H_4O_2^+$, 0.76 % of the total HRMS) and *m/z* 73 (mainly $C_3H_5O_2^+$, 1.09 % of the total HRMS), which are characteristic fragments associated with levoglucosan, a tracer compound of biomass burning particles (Kumar et al., 2022; Qin et al., 2017). Correlations between BBOA and these two tracer ions were indeed tight (0.71 with $C_2H_4O_2^+$and 0.82 with $C_3H_5O_2^+$). A notably positive correlation between BBOA and K^+ (Fig. 3b) further supports its BB origin as K^+ is also a common BB emission tracer (Yu et al., 2018). Note the BBOA here had a relatively higher O/C ratio of 0.61 than those identified in

previous offline AMS measurements, such as Yangzhou (0.45) (Ge et al., 2017), Beijing, China (0.59) (Qiu et al., 2019), and Marseille, France (0.54) (Bozzetti et al., 2017), suggesting the presence of partially aged BBOA species in this factor.

The other two factors are secondary. OOA1 was less oxidized with a O/C of 0.39 and OOA2 was more oxygenated with the highest O/C of 0.65 among all factors. OOA1 had characteristic fragments at *m/z* 29 (CHO^+) and *m/z* 43 (mainly $C_2H_3O^+$) while OOA2 had the least fraction of oxygen-free $C_xH_y^+$ ions (28.5 %) but the largest fraction of oxygenated ions (32.8 % of $C_xH_yO_1^+$ and 18.9 % of $C_xH_yO_2^+$) among the four factors. OOA2 correlated well with CO_2^+ (*m/z* 44) (*r* of 0.81), a characterisitic ion of highly oxygenated carboxylic/dicarboxylic acids. Moreover, OOA2 had the highest N/C of 0.095 as well as those of $C_xH_yN^+$ (9.1 %) (such as CH_2N^+, CHN^+ and CH_4N^+) and $C_xH_yO_zN^+$ (3.8 %) (such as $CHON^+$, CH_2NO^+ and CH_4NO^+), indicating the presence of amines and amino acids correspondingly (Ge et al., 2024). Besides, the N/C level of OOA2 is close to that of fogwater observed in Fresno, indicating the aqueous phase reactions are likely an source of those nitrogen-containing ions in OOA2 (Kim et al., 2019). In addition, sulfur-containing organic ions (such as CH_2S^+, $CH_3SO_2^+$ and CHS^+) were almost exclusively present in OOA2 and in a significant fraction (2.7 %), as such ions were strongly associated with aqueous/heterogenous reactions (Zorn et al., 2008; Huang et al., 2020; Petters et al., 2021; Mcneill, 2015), reassuring that OOA2 was very likely linked with aqueous/heterogenous formation pathway.

The time series of mass contributions of the four factors are shown in Fig. 1d, and significant differences can be observed during the two sampling seasons, as can be seen clearly in Fig. 3a. HOA was a significant source in both SS and CS, and as expected, it was higher during daytime due to the stronger traffic activities. BBOA was much less important than HOA, but its contribution during CS was obviously more than that during SS (12.5 ~ 13.0 % vs. 7.2 ~ 7.8 %), and accordingly, HOA contribution was slightly larger during SS than during CS (38.0 ~ 41.7 % vs. 29.9 ~ 36.8 %). It is worthy to mention that, BBOA can be more important than HOA, such as in Bejing during autumn polluted period (38.3% of WSOA) (Hu et al., 2020) , in Delhi, India (31-34%

of WSOA) (Bhowmik et al., 2024), and in urban and rural Catalonia, Spain (up to 26% of WSOA) (Veld et al., 2023). In general, the dominance of SOA in WSOA observed here was consistent with most offline AMS studies aformentioned, except that POA was found to dominate WSOA in Delhi, India (Bhowmik et al., 2024). However, mass contributions of the two individual SOA factors in different seasons in this study were strikingly different. OOA1 occupied nearly half of the total WSOA (47.5 ~ 49.8 %) while contributions of OOA2 were only 3.0 ~ 5.0 % during SS; on the other hand, OOA2 occupied 38.6 ~ 43.5 % of WSOA mass while those of OOA1 were down to 11.6 ~ 14.1 %. The much larger OOA2 fraction during CS explains its overall high oxidation degree depicited in Fig. 2. These results are well consistent with our previous studies, as we show that during summer in Nanjing, photochemical reactions dominate the SOA formation and yield relatively less oxygenated OA (Xian et al., 2023; Wang et al., 2022b), while during cold seasons, aqueous formation of SOA becomes more important which can generate highly oxygenated OA (Wu et al., 2018). The air temperature (a solar radiation indicator) and ozone (a photochemical product) both correlated positively with OOA1 but negatively with OOA2 (Fig. 3b), further verifying the dominance of photochemical production of OOA1 not OOA2. As is well known, particulate nitrate was strongly associated with heterogenous reactions and gas-to-particle partitioning favored by low temperature and high RH especailly during CS, and indeed, OOA2 correlated much tighter with NH_4NO_3 than OOA1 did.

3.2 Optical properties

3.2.1 Light-absorbing properties of WSOC and MSOC

The average light absorption coefficients of BrC in WSOC and MSOC in 300 ~ 700 nm during daytime and nighttime of SS and CS are illustrated in Fig. 4a. As expected, the values all exponentially decreased as a function of wavelength. The calculated AAE values are listed in Table 1. It is interesting to find that the WSOC AAE had no significant difference between SS and CS (6.35 vs. 6.43), while that of MSOC AAE appeared to be notable (5.99 vs. 6.89); Compared with the MSOC AAE, the

WSOC AAE was higher during SS but smaller during CS. The AAE values obtained here are slightly smaller than those reported in Beijing (7.3 ~ 7.5 of WSOC) (Du et al., 2014; Chen et al., 2016), comparable to that in Guangzhou (6.7 of WSOC) (Fan et al., 2016). Note Chen and Bond (2010) reports that particles generated from smoldering of various types of wood exhibit a AAE of 6.9 ~ 11.6 (MSOC); Lambe et al.(2013) shows that lab-generated secondary BrC possesses a AAE of 5.2 ~ 8.8 (MSOC). Compared with these values, our measured AAE values (<7) here probably suggest a dominance of secondarily formed BrC for both WSOC and MSOC. This can be verified by Fig. 3a for WSOC, as indeed it was dominated by SOA particularly during nighttime in both seasons. However, the large difference in WSOA chemical composition in different seasons (especially SOA proportions) did not result in a large difference in WSOC AAE, demonstrating clearly the non-correspondence of chemical species to light-absorbing species (a.k.a., BrC). On the contrary, for MSOC, the relatively large difference of MSOC AAE in different seasons likely reflect the distinction of BrC species but not necessarily chemical constitution. The light absorption coefficients at 365 nm (Abs_{365}) are listed in Table 1 too. The average $Abs_{365,\ WSOC}$ during CS (4.87 M m^{-1}) was approximately 2.15 times that of SS (2.27 M m^{-1}), and that of MSOC during CS (4.97 M m^{-1}) was also much larger than that during SS (3.64 M m^{-1}); Nighttime values were higher than those in daytime expect for WSOC during CS. For the same set of samples, $Abs_{365,\ MSOC}$ values were typically larger than $Abs_{365,\ WSOC}$ except that CS daytime $Abs_{365,\ MSOC}$ was slightly smaller than $Abs_{365,\ WSOC}$ (4.65 vs. 4.89 M m^{-1}). Scatter plots of Abs_{365} versus WSOC (and MSOC), and $Abs_{365,\ WSOC}$ versus $Abs_{365,\ MSOC}$ for the four series of samples are given in Fig. S5. The correlations were generally well especially those of WSOC and MSOC (r > 0.80), suggesting that there is a large overlap of extracted species between WSOC and MSOC, as well as their BrC constituents.

Regarding the MAE at 365 nm (MAE_{365}), $MAE_{365,\ WSOC}$ during CS (0.75 $m^2\ g^{-1}$) was higher than that during SS (0.55 $m^2\ g^{-1}$), indicating its stronger light absorption ability during CS; however, the $MAE_{365,\ MSOC}$, unlike $Abs_{365,\ MSOC}$, was smaller during CS than that during SS (0.50 vs. 0.72 $m^2\ g^{-1}$). Besides, MAE_{365} values for both WSOC

and MSOC were slightly larger during nighttime than those during daytime in both seasons. Compared to previous winter studies, the $MAE_{365, WSOC}$ in Nanjing here was lower than that in Beijing (1.21 ~ 1.26 $m^2 g^{-1}$) (Du et al., 2014; Chen et al., 2016; Li et al., 2020), similar to our earlier observation in Yangzhou (0.75 $m^2 g^{-1}$), but the $MAE_{365, MSOC}$ appears to be less than that in Yangzhou (1.12 $m^2 g^{-1}$)(Chen et al., 2020). To further explain the low MAE_{365} observed here, we investigated the air mass origins of our samples collected in different periods via back trajectory analysis (at an altitude of 200 m and 24 hours backwards) using the MeteInfo (Version: 3.0.0) (Wang, 2019). As shown in Fig. S6, only a limited fraction of air mass trajectories passed through sea and coastal areas (clusters 4 and 5, 27.05 % during daytime and 29.54 % during nighttime) during SS, while during CS, proportions of trajectories that intercepted sea/costal air increased to 79.80 % (clusters 1, 2 and 3 during daytime) and 69.44% (clusters 2, 3 and 4 during nighttime), respectively. Note the air masses during CS are somewhat unusual as typically they mainly originate from inland regions (Wu et al., 2019b), which might cause the low MAE_{365} observed in this work as particles affected by marine air can be less light-absorptive than those influenced by inland air (Li et al., 2022a).

Saleh (2020) proposes a method that uses the MAE_{405} (MAE at 405 nm) – AAE two-dimension space to assess the light-absorbing ability of BrC, as shown in Fig. 4b. The majority of samples in this study fall into the regime of W-BrC (weakly light-absorptive BrC) with a few MSOC samples locating in the VW-BrC (very weak BrC) regime, which are similar to a few other observations (Zhou et al., 2021; Xu et al., 2022). The BrC in MSOC seemed to cover a broader region than it in WSOC, indicating that the MSOC BrC might contain a wider array of species and/or originate from more diverse sources/processes. Daytime/nighttime difference of MSOC BrC was also more obvious than that of WSOC BrC.

At last, we estimated the SFE values of WSOC and MSOC in the range of 300–700 nm, considering the actual visible light wavelength as well as the negligible light absorption above 700 nm of BrC. As summarized in Table 1, the mean SFE_{MSOC} (2.43 W g^{-1}) during SS was higher than that of WSOC (2.20 W g^{-1}), but it became smaller

during CS (2.23 W g^{-1}) and was much lower than that of WSOC (3.24 W g^{-1}). The SFE_{WSOC} values in both SS and CS were lower than that in Beijing (4.6 ± 1.7 W g^{-1} in summer and 6.2 ± 2.0 W g^{-1} in winter), especially in CS (Deng et al., 2022). For both WSOC and MSOC, SFE values during nighttime were slightly larger.

3.2.2 Source apportionment of light absorption of WSOC

In Sect. 3.1.2, sources of WSOA were identified and quantified, herein we applied a multiple linear regression (MLR) algorithm to apportion the light absorption of WSOC to these sources. The scatter plot of reconstructed $Abs_{365, WSOC}$ versus measured values are shown in Fig. S7. The fitted slope is 1.06 with a Pearson's *r* of 0.90, verifying the robustness of this method on our dataset. The calculated regression coefficients, representing the factors' MAE_{365} values (m^2 g^{-1}) are listed in Table 2. Compared to our earlier results (Chen et al., 2020b), the HOA MAE_{365} (0.71 m^2 g^{-1}), was much less than that in Yangzhou (1.46 m^2 g^{-1}), while the BBOA MAE_{365} values were similar (0.71 vs. 0.77); MAE_{365} values of OOA1 (0.12 m^2 g^{-1}) and OOA2 (0.83 m^2 g^{-1}) were very close to the two SOA factors in Yangzhou (0.11 and 0.85 m^2 g^{-1}). However, here the less oxygented OOA1 has the small MAE_{365} while in Yangzhou, the more oxygenated SOA has the similar MAE_{365} as OOA1, and *vice versa* for the other pair. This work finds that the more oxidized SOA has a stronger light absorption ability, opposite to that reported in Yangzhou. Nevertheless, the two findings are not contradictory with each other, as atmospheric ageing can lead to either photo-enhancement or photo-bleachment, dependent upon the precursors. For instances, aqueous oxidation of BBOA can increase (Gilardoni et al., 2016) yet conversely aqueous processing of fossil fuel combustion OA can decrease the light absorptivity of OA (Wang et al., 2021). As discussed in Sect. 3.2.1, the unusual air masses during CS in this work clearly indicate different precursors from those in Yangzhou.

The average contributions of HOA, BBOA, OOA1 and OOA2 to $Abs_{365, WSOC}$ across the whole campaign were 33.05 %, 15.49 %, 6.00 % and 45.46 %, respectively (Table 2). Figure 5 further presents contributions of the factors under different scenarios. Compared with their mass contributions shown in Fig. 3a, during SS, the dominant

contributor of light absorption became HOA (daytime 63.7 %, nighttime 55.6 %), and contributions of BBOA and OOA2 both increased relative to their mass fractions; while OOA1's contribution was largely reduced to 15.0 ~ 16.2 % due to its small MAE_{365}. Previous studies have consistently identified coal combustion (Fan et al., 2016; Li et al., 2019; Song et al., 2019) and traffic emissions (Hecobian et al., 2010) as significant contributors to BrC, together with our results here, highlighting the substantial impact of anthropogenic fossil fuel combustion on atmospheric visibility. During CS, OOA2 dominated the light absorption (daytime 50.7 %, nighttme 63.0 %) owing to its large mass contribution as well as large MAE_{365}; OOA1 became a very minor contributor (2.1 ~ 2.8 %), HOA contribution decreased while BBOA contribution increased relative to their mass fractions. Overall, we find that primary fossil fuel combustion emissions govern water-soluble BrC light absorption during SS especailly during daytime, while during CS, secondary highly aged species (likely from aqueous/heterogenous reactions) dominates, especially during nighttime.

To further explore the impact of atmospheric ageing on BrC, we plotted MAE_{365} as a function of O/C in Fig. 6. Interestingly, during SS, MAE_{365} generally decreased with the increase of O/C, especially in daytime as its fitted slope of -1.56 was over 2 times that of nighttime (-0.76). On the other hand, MAE_{365} showed an increasing trend against O/C during CS, particularly in nighttime as the fitted slope was 1.43, larger than that of daytime (1.12). These results further supports our earlier findings and underscore that during summer photochemical reactions can lead to photo-bleachment of aerosols while during cold seasons aqueous/heterogenous reactions might dominate the secondary formation and lead to photo-enhancement; clearly, photochemical oxidation and aqueous/heterogenous reactions are more active during daytime and nighttime, respectively, consistent with the slopes in Fig. 6. Also, photochemcially produced SOA was often less or moderately oxygenated and that from aqueous/heteregenous oxidation was more oxidized, and there is a turning point at O/C of 0.45 ~ 0.5 in the MAE_{365}-O/C plot. Many studies have shown that aqueous reactions are a source of BrC (e.g., Li et al. (2022c), Laskin et al. (2015) and Ye et al. (2019)), but evidence also shows that

further aqueous ageing of BrC can lead to photo-bleaching (e.g., Zhao et al. (2015) and Lei et al. (2025)), therefore a certain O/C turning point can exist if the OA evolution was governed by a certain process. The real atmospheric processes are however complicated, such O/C points might be less clear. Nevertheless, similar points were indeed observed previously (Zhong et al., 2023; Jiang et al., 2022).

3.2.3 Fluorescent properties of WSOC and MSOC

The fluorescence indices like HIX, BIX and FI, can infer the types and sources of dissolved organic matter (DOM) in aquatic systems and soils (Lee et al., 2013; Huguet et al., 2009). Recently, these indices have been employed to investigate sources and aging processes of atmospheric OA (Fu et al., 2015; Qin et al., 2018; Deng et al., 2022; Murphy et al., 2013). Here, we calculated these indices for both WSOC and MSOC.

HIX represents the degree of humification, and a high HIX means high aggregation, C/H ratio and aromaticity of the organics (Zsolnay et al., 1999; Mcknight et al., 2001; Birdwell and Engel, 2010), thus it normally increases upon ageing (Fan et al., 2019; Murphy et al., 2013). In this study, HIX of WSOC during SS and CS were on average 3.34 and 4.68, respectively (Table 3), much less than the HIX levels in aquatic or soil DOM (Dong et al., 2017), suggesting an overall low aromaticity of atmospheric OA in Nanjing. As a comparison, the WSOC HIX are higher than those in Colorado, USA (2.42) (Xie et al., 2016) and Tianjin, China (2.73 and 2.22) (Deng et al., 2022), but significantly lower than that in Nanjing during 2017-2018 (7.07) (Xie et al., 2020). An earlier study proposes the HIX ranges of 1.4-5 for fresh SOA and 4.2-6.1 for aged SOA (Lee et al., 2013). Despite influences of other primary sources, the average HIX during SS did fall in the fresh SOA range and the value during CS entered the edge of aged SOA, in line with the oxidation degrees of OA (Fig. 2a) and mass proportions of fresh/aged SOA factors (namely, OOA1/OOA2) (Fig. 3a) during different seasons. The average HIX of MSOC (2.72 and 3.48) were lower than those of WSOC in both seasons, indicating that HULIS with high aromaticity are preferentially soluble in water.

FI is indicative of the relative contributions of terrestrial and biogenic sources while BIX, in contrast to HIX, can be treated as a freshness index. A fluorophore is

595 often associated with high aromaticity if FI is low (Fu et al., 2015), and a high BIX
596 indicates a high content of freshly released organics (such as biological or microbial
597 derived species) (Wen et al., 2021; Huguet et al., 2009; Murphy et al., 2013). The
598 average WSOC BIX values during SS and CS were determined to be 0.84 and 0.88,
599 respectively, with corresponding FI of 1.91 and 1.90 (Table 3), and the corresponding
600 MSOC BIX were 0.90 and 0.96, and MSOC FI were 2.27 and 2.11, respectively.
601 Compared with results during 2017-2018 in Nanjing, BIX and FI values of WSOC were
602 similar, yet those of MSOC here were larger (Xie et al., 2020). Figure 7 shows the
603 measured data in the HIX-FI and HIX-BIX diagrams along with results from a few
604 other studies. It can be seen that, almost all BIX values distributed in the range of 0.6 ~
605 1 (Huguet et al., 2009) and FI values distributed within 1.6 ~ 1.9 (Mcknight et al., 2001),
606 suggesting that OA in both seasons was influenced by a mix of terrestrial and
607 microbial/biogenic sources. For both WSOC and MSOC, BIX was slightly higher
608 during CS than during SS, attributing to the fact that OA during CS contained more
609 aged SOA species. Nearly no difference for WSOC FI during different seasons were
610 observed, but the MSOC FI during CS was slightly lower than that during SS, meaning
611 that MSOC during CS had a high aromaticity as expected. In addition, BIX and FI
612 values during nighttime were marginally higher than those during daytime in all cases.

613 **3.2.4 Identification of key fluorophores of WSOC and MSOC**

614 The 3D EEM-PARAFAC analysis was adopted to identify the key fluorophores of
615 BrC, with results in Fig. 8 and Fig. S8. Four components were resolved for both WSOC
616 and MSOC. For WSOC, C1 exhibited a peak at Ex = 230 nm and Em = 374 nm,
617 identified as less oxidized HULIS typically associated with combustion sources. Its
618 contribution was only 4.9 % during SS but increased to 19.2 % during CS (Fig. S8a).
619 C2 had a prominent peak at Ex = 230 nm and Em = 396 nm and a second peak at Ex =
620 320 nm and Em = 396 nm, classified as a HULIS-related component too, as the dual-
621 peak distribution of fluorescence spectrum is often associated with HULIS (Coble,
622 1996; Murphy et al., 2011; Yu et al., 2015); its second peak indicates the abundance of
623 compounds with condensed aromatics, conjugated bonds, and non-linear rings (Matos

et al., 2015), likely a mix of primary and secondary sources. C2 contribution was thus comparable during different seasons (37.5 % vs. 38.6 %), and it seemed to be more important in nighttime than in daytime (44.0 % vs. 26.9 % during SS, and 41.4 % vs. 34.8 % during CS). C3 component, with a peak at Ex = 240 nm and Em = 446 nm, was considered as a highly oxidized HULIS component, relevant with secondary processes (Cheng et al., 2016; Cao et al., 2021). Hawkins et al. (2016) and Aiona et al. (2017) reported fluorescent pattern of products from aqueous-phase reaction of aldehydes with ammonium sulfate or amines (Ex < 250/300 nm and Em > 400 nm) well matching the pattern identified here. As discussed earlier, aqueous/heterogenous reactions contributed to WSOA, especailly during CS; correspondingly, C3 contribution was indeed much higher during CS than during SS (24.1 % vs. 14.7 %). C4, with a prominent peak at Ex = 230 nm and Em = 308 nm and a second peak at Ex = 275 nm and Em = 305 nm, was characterized as a protein-like component (Yan and Kim, 2017; Wu et al., 2019a; Chen et al., 2020b). C4 was the single largest contributor (42.9 %) during SS particualy during daytime (55.0 %), but became the least during CS (18.0 %).

Similarly for MSOC, three HULIS-related fluorophores (C1 ~ C3) and one proteinaceous fluorophore (C4) were separated (Fig. 8b). The spectral signatures between the two series of fluorophores were slightly different, with the MSOC peak excitation and emission wavelengths being a bit larger than those of WSOC, especailly for C2 and C3. Figure S8b shows contributions of the different components to MSOC fluorescene. C1 was much more important in MSOC (26.6 % in SS and 39.2 % in CS) than in WSOC, and became the largest contributor of MSOC during CS; summed C2 and C3 contributions (30.7 % in SS and 37.0 % in CS) were on the other hand much less than in WSOC; C4 remained to be the largest (42.6 %) similar to that in WSOC during SS. The increased contributions of the protein-like fluorophore (C4) during SS in both WSOC and MSOC were likely due to its major origin of biological activities, which can be enhanced by the relatively high temperatures during SS (Fan et al., 2020); this is likely the reason that C4 contributions during daytime were higher than those during nightime in both SS and CS. Furthermore, some studies (Barsotti et al., 2016;

Chen et al., 2021; Chen et al., 2020b; Cao et al., 2021; Deng et al., 2022) also point out that C4 not only contains proteinaceous species from biological activities but also certain PAHs or phenolic substances from fossil fuel and/or biomass burning, especially in urban aerosols. Probably, the proteinaceous species dominated the fluorescence during SS for both WSOC and MSOC, while during CS PAHs and phenolic compounds became more important and they might prefer to dissolve in methanol therefore lead to its higher contribution in MSOC than in WSOC (23.8 % vs. 18.0 %). Different solubilities of HULIS components in water and methanol may partially lead to their different contributions in WSOC and MSOC.

3.3 Molecular composition of organics

3.3.1 Overview of identified molecules

We classified the identified molecular formulas of organics (here MSOA) via UPLC-QTOF-MS analysis into 8 categories, namely CH, CHO, CHN, CHS, CHON, CHOS, CHNS, and CHONS. Overall, the negative (ESI^-) and positive (ESI^+) ion modes identified 466 ~ 865 and 644 ~ 1065 formulas, respectively (details in Table S1). Figures S9 and S10 shows the number and signal fractions (relative abundances of signal intensities) of different classes of compounds, respectively.

Under ESI^+ mode, CHON compounds were the most abundant species in term of the number fraction – nearly half during SS (daytime 50.5 % and nighttime 46.9 %), and over half during CS (daytime 54.1 % and nighttime 55.1 %), and the abundance of its signal was even more prevailing – over half in all cases and up to 67.7 % during SS daytime; the second abundant species were CHO compounds, occupying 23.0 ~ 30.6 % of the total number of molecules and 15.4 ~ 21.9 % of the total signal intensity; CHONS and CHN species were the other two relatively abundant classes – together occupying ~ 20 % (number fraction) and ~ 10 ~ 24 % (signal fraction) of total identified compounds; contributions of other four classes of compounds were very minor, in terms of both number and signal intensity. Relatively, under ESI^- mode, CHO compounds marginally prevailed over CHON compounds in number (36.2 ~ 44.4 % vs. 32.6 ~

38.0 %), but during CS their signal fractions were still lower (33.3 ~ 35.1 % vs. 39.3 ~ 46.5 %). More enrichment of CHO compounds in ESI^- than in ESI^+ is consistent with a previous work (Lin et al., 2012) as these compounds most likely contain carboxyl groups and are easily deprotonated in ESI^- mode. Number fractions of CHONS compounds in ESI^- mode were ~5 ~ 10% more than those in ESI^+ mode, while the most contrasting difference was that CHN compounds were rarely detected in ESI^+ mode, and instead CHOS compounds that were negligible in ESI^- mode could be effectively detected in ESI^+ mode (3.9 ~ 4.8 % in number) and their signal fractions were more significant (6.4 ~ 17.4 %).

3.3.2 CHO compounds

For the detected CHO compounds, we plotted them in the van Krevelen (VK) diagrams according to their H/C and O/C ratios in Fig. 9. Most molecules had the O/C ratios < 0.5, but a broad distribution of H/C ratios (0.5 ~ 2.0). Molecules with high H/C ratios (≥ 1.5) and low O/C ratios (≤ 0.5) (Region A) were typically associated with aliphatic compounds, while those with low H/C ratios (≤ 1.0) and low O/C ratios (≤ 0.5) (Region B) are usually assigned to oxygenated aromatics (Kourtchev et al., 2014). We further calculated the Xc values of all CHO compounds to investigate their molecular structures in Fig. 9. Clearly, saturated aliphatic CHO compounds (Xc < 2.5) were most abundant (323 out of 418 in ESI^+ mode, and 315 out of 481 in ESI^- mode) and mainly distributed in Region A. Appreciate number of unsaturated compounds particularly those with benzene ring or naphthalene ring structures (2.5 <Xc <2.8), distributed across from H/C of 0.5 to 1.75 but with O/C < 0.5 in ESI^- mode and from H/C of 0.1 to 1.75 but with a few in the side of O/C > 0.5.

The oxygenation state (OS_c) (Kroll et al., 2011) (defined as 2*O/C - H/C), is another metric to assess the ageing/oxidation degree of a compound. Figure 10 illustrates the dependence of OS_c on carbon number for all CHO compounds. The molecules had a broad coverage of OS_c (-2 to +2) and carbon number (up to 50). Kroll et al. (2011) grouped the compounds into different origins according to their OS_c and C numbers, including fossil fuel combustion HOA, BBOA, semi-volatile oxygenated OA

(SV-OOA, typically less-oxidized) and low-volatility oxygenated OA (LV-OOA, typically more-oxidized), as marked in Fig. 10. Obviously, for both ESI^- and ESI^+ modes, a large portion of compounds belonged to HOA and BBOA. In ESI^+ mode, a significant portion of molecules located in the BBOA region, while in ESI^- mode, more molecules tended to be found in the HOA region, and even more molecules located within HOA regime during CS than during SS (Figs. S11 and S12), indicating large influences from anthropogenic emissions. Besides, the number of nighttime LV-OOA molecules was more than that of daytime particular during CS, acting as a supporting evidence of aqueous/heterogeneous reactions.

3.3.3 CHON and CHN compounds

We mapped the detected CHON compounds colored by Xc in the VK diagrams shown in Fig. 11. The compounds were sorted into different series according to the functional groups as well. For ESI^+ mode (Fig. 11a), the compounds containing a -NO moiety were dominant and a majority of CHON compounds were saturated with $Xc < 2.5$. Among them, $C_6H_{15}NO(CH_2)_n$ might be N,N-diethylethanolamine homologous compounds, and $C_6H_{15}NO_2(CH_2)_n$ might be diisopropanolamine homologous compounds, as both compounds possess lone pair electrons, prone to positive charge (Ge et al., 2011). Unsaturated CHON compounds with $X_C \geq 2.5$ located in the bottom-left corner, such as $C_5H_5NO(CH_2)_n$, $C_7H_7NO(CH_2)_n$, $C_8H_7NO(CH_2)_n$, and $C_9H_7NO(CH_2)_n$, likely homologous compounds of hydroxypyridine, benzamide, 4hydroxy-benzene acetonitrile, and hydroxyquinoline, respectively (Ma and Hays, 2008; Wang et al., 2020). In ESI^- mode, the compounds scattered wider than those in ESI^+ mode in the VK plot (Fig. 11b), and the majority of them contained one or two nitrogen atoms. Over 25 % of the CHON formulas can be classified as monocyclic or polycyclic compounds with $Xc \geq 2.5$ (even up to 68 % during SS daytime; inferred from Figs. S13 and S14). The identified series of homologous compounds mostly situated in the bottom-left corner and also with $Xc \geq 2.5$, such as $C_6H_5NO_3(CH_2)_n$, $C_6H_5NO_4(CH_2)_n$, $C_8H_7NO_3(CH_2)_n$, $C_8H_7NO_4(CH_2)_n$, and $C_{10}H_7NO_3(CH_2)_n$, likely nitrophenol, nitrocatechol, nitroacetophenone, nitrophenylacetic acid, and

nitronaphthol homologues, respectively (Wang et al., 2018b; Song et al., 2019; Lin et al., 2017; Lin et al., 2015).

As stated in Sect. 3.3.1, CHN compounds were only enriched in ESI^+ mode. The scatter plot of H/C versus N/C of these compounds is depicted in Fig. 12 (results of different periods are shown in Fig. S15). Similarly, they are colored by Xc and sorted into a number of different series. Most of these compounds were amines with one or two N atoms. The series of aliphatic amines and other monocyclic species with $X_C <$ 2.71 mostly located in upper part of the plot, including $C_6H_{15}N(CH_2)_n$, $C_5H_{11}N(CH_2)_n$ and $C_6H_{12}N(CH_2)_n$, $C_4H_6N_2(CH_2)_n$, $C_5H_6N_2(CH_2)_n$, $C_7H_6N_2(CH_2)_n$, and $C_{11}H_{17}N(CH_2)_n$. Note the presence of 2 N-heterocyclic species was a sign of presence of BBOA (Wang et al., 2017). The series of $C_{10}H_9N(CH_2)_n$ (1N-PAHs) with $X_C \geq 2.71$ may represent the aminonaphthalene homologues (Ge et al., 2011), likely from initial burning of carbonaceous materials (Mao et al., 2022).

3.3.4 CHOS and CHONS compounds

Among the CHOS formulas (only significant in ESI^- mode), ones with O/S ratios ≥ 4 were classified as organosulfates (OSs), which were the most abundant type (Table 4). Its number fractions were particularly high during CS (daytime 54.3 %, nighttime 68.6 %), reiterating the importance of aqueous SOA formation during CS. For the CHONS compounds, in ESI^- mode, 5.3 ~ 12.5 % of the formulas had O/(4S+3N) ratios ≥ 1, allowing them to be assigned to $–OSO_3H$ and $–ONO_2$ groups, namely nitrooxy-organosulfates (nitrooxy-OSs) (Wang et al., 2018a); while in ESI^+ mode, 9.8 ~ 11.8% of total CHONS formulas were apportioned as nitrooxy-OSs (Table 4).

3.4 Machine learning assisted identification of key BrC molecules

To enhance the robustness of ML analysis, we first incorporated all detected compounds without assigned molecular formulas of both positive and negative modes (4953 formulas, ESI^+: 2863, ESI^-: 2090) into the ML model. After ML analysis, a total of 1477 molecules (ESI^+: 795; ESI^-: 682) were found to have positive values for both IncNPu_val and IncMSE_val. Among them, 1051 molecules (ESI^+: 420; ESI^-: 450)

were assigned corresponding molecular formulas; and furthermore, a total of 149 compounds with 0.5<DBE/C<0.9 (ESI^+: 52; ESI^-: 97) were chosen. By comparing with the database, we finally proposed 31 compounds (ESI^+: 18, ESI^-: 13) as the key BrC species; details regarding their molecular formulas and proposed structures, etc., are summarized in Table S2. These species are relevant with 4 out of 8 identified types of compounds (CH, CHO, CHN and CHON) (Fig. 13). To the best of our knowledge, 6 out of the 31 species (4-methylcoumarin, urocanate, 3-hydroxybenzoic acid, chrysin, 2-hydroxypyridine and 4-hydroxyacetophenone) have not been reported before as important BrC species.

Two PAHs (acenapthylene and fluoranthene, belonging to CH category) in ESI^+ mode were identified, consistent with that PAHs are known important BrC (Aurell et al., 2015; Kuang et al., 2021).

Twelve CHO compounds (5 in ESI^+ mode and 7 in ESI^- mode) were identified. In ESI^+ mode, 9-fluorenone and benzanthrone belonging to oxyheterocyclic PAHs (O-PAHs), are known as important BrC chromophores (Kuang et al., 2023); scopoletin is also known as a light-absorbing compound (Zhang, 2018); phthalic anhydride is an oxygen-containing heterocyclic compound. A previous study reports that methanol (the solvent used here) might react with conjugated carbonyl species (such as phthalic anhydride, maleic anhydride, and maleimide) (Chen et al., 2022), thereby affecting the light absorption of relevant BrC species, further studies are needed to verify phthalic anhydride as a key chromophore. In ESI^- mode, a pair of quinone isomers (1-hydroxyanthraquinone and 2-hydroxyanthraquinone) were resolved, in agreement with Kuang et al. (2023), which identified 1-hydroxyanthraquinone as a BrC chromophore in Beijing; 1-hydroxypyrene is a hydroxylated PAHs , also proven as a BrC before (Huang et al., 2022).

The identified seven CHN compounds (exclusively in ESI^+ mode) included 4 N-heterocyclics, 2 nitro-PAHs, and 1 quinoline compound. It is well known that biomass burning (BB) release a lot of BrC species. As mentioned earlier, CHN compounds are abundant in BB emissions (such as agricultural waste burning and forest fires (Laskin

et al., 2009)); small N-containing heterocyclic compounds with one or two aromatic rings, can be effectively produced from thermal decomposition of plants (Ma and Hays, 2008), and high temperature pyrolysis of CHN compounds and N-containing plant materials, can result in N-PAHs (Lin et al., 2016). Therefore, identification of the CHN species here as key BrC chromophores are well justified.

The remaining confirmed BrC molecules included 10 CHON compounds (4 in ESI^+ mode and 6 in ESI^- mode). For ESI^- mode, 3-hydroxyanthranilic acid is an amino phenolic compound $^-$, and the rest five compounds are all nitrophenols, well known as BrC (Li et al., 2020). Another amino phenolic compound, 2-aminophenol was identified in ESI^+ mode. Previously, efficient light absorption at 275 nm of 2-aminophenol has been reported, which can be further enhanced in the presence of Fe^{3+} due to formation of oligomers (Al-Abadleh et al., 2022). For acridone in ESI^+ mode, earlier studies have shown that acridine exhibits increased light absorbance in the wavelength range of 260 ~ 320 nm under irradiation in N_2, air, or O_2; additionally, a deep yellow layer forms on the surface, indicating the production of light-absorbing products, which was identified as acridone (Negron-Encarnacion and Arce, 2007).

For the BrC species identified here, most species contain at least one benzene ring (such as PAHs and NACs) except two compounds (2-hydroxypyridine and urocanate) with other aromatic ring structures. This is reasonable as organic compounds with benzene or other aromatic rings (with conjugated double bonds) are known to be strong light-absorbing. The -OH and -COOH groups on the benzene ring can enhance ultraviolet light absorption at near-UV wavelengths (Jacobson, 1999); The $-NO_2$ group can further increase light absorbance at longer wavelengths (Jacobson, 1999). Our identified BrC list does include compounds with such functional groups. Note some nitrogen-containing heterocyclic compounds, are usually secondary products of aqueous reactions between carbonyl compounds (such as glyoxal and methylglyoxal) and amines or ammonium (Powelson et al., 2014); thus identification of them here as key BrC species is also a supporting evidence of the occurrence of aqueous reactions.

4 Conclusions

This work performed a comprehensive investigation on the chemical and optical properties of BrC in ambient $PM_{2.5}$ samples. Regarding the chemical properties, it was found that methanol was able to extract more OC than water (~82.0% vs. 49.5 ~ 61.3% of total OC). The WSOA was composed of two primary factors relevant with fossil fuel combustion (HOA) and biomass burning (BBOA), and two SOA factors (a less oxidized OOA1 and a highly oxygenated OOA2). During CS, OOA2 was abundant (38.6 ~ 43.5 %) while during SS OOA1 was abundant (47.5 ~ 49.8 %); HOA was also an important contributor in both seasons (29.9 ~ 41.7%) but BBOA contribution was relatively minor (7.2 ~ 13.0 %). Further analyses reveal that OOA1 was mainly associated with photochemical reactions while OOA2 was strongly linked with aqueous/heterogeneous reactions.

Regarding the optical properties, our observation shows that $Abs_{365,\ MSOC}$ was typically larger than $Abs_{365,\ WSOC}$, but though $MAE_{365,\ MSOC}$ was still larger than $MAE_{365,\ WSOC}$ during SS, it became smaller than the $MAE_{365,\ WSOC}$ during CS, likely owing to that the air mass trajectories during CS significantly intercepted sea/coastal air. The light absorbing abilities of both WSOC and MSOC were weak, but our observations suggest that aqueous oxidation can lead to significant photo-enhancement, therefore the light absorption of WSOA was dominated by OOA2 (50.7 ~ 63.0 %) during CS; while photochemical oxidation could cause a photo-bleaching effect and therefore the contribution of OOA1 to WSOA absorbance was small (15.0 ~ 16.2 %), and HOA contribution was prevailing during SS (55.6 ~ 63.7 %). PARAFAC analysis on the fluorescent spectra of WSOC and MSOC both resolved four key components, including three HULIS component and one protein-like component. HIX, BIX and FI indices also suggest that both WSOC and MSOC originated from a mix of terrestrial and microbial/biogenic sources.

The molecular analysis determined 644 ~ 1065 molecules in ESI^+ mode and 466 ~ 865 molecules in ESI^- mode. Overall, CHON compounds were the most abundant type especially in ESI^+ mode, while CHO compounds slightly exceeded CHON compounds

in number but were still lower in signal intensity. CHN compounds was the third important class and only detectable in ESI^+ mode. The VK diagrams further demonstrate the different aromaticity equivalent (Xc) values and evolution pathways of the different classes of compounds. In addition, significant presence of organosulfates and nitroxy-organosulfates in CS samples especially during nighttime re-affirm the importance of aqueous-phase oxidation during CS. Finally, based on the molecular characterization and light absorption measurement results, we applied the ML RF algorithm to identify the key BrC molecules, and we successfully identified 31 key species, including mainly the PAHs, oxyheterocyclic PAHs (O-PAHs), quinones and N-containing compounds; some of them are newly identified.

Of course, our study has some limitations. One limitation is that no source apportionment was conducted on MSOA due to technical difficulties, therefore a full closure between emission sources and optical properties of total OA is incomplete; development of proper method should be the subject of our future work. Besides, our findings here expand the understanding on chemical (both bulk and molecular level) and optical properties (both light absorption and fluorescence) of BrC, and are valuable to evaluate its impact on air quality and radiation balance; yet our practice with ML analysis here serves only as a valuable attempt, more studies are clearly needed.

Nevertheless, the ML approach has demonstrated its great potential in identifying new key BrC species (such as 4-methylcoumarin, urocanate, etc here) as well as reaffirming the importantance of known key BrC molecules (such as the nitrogen-containing aromatic molecules); such ML-identified list can be a useful reference for future studies. Of course, since there are multiple types of ML algorithms (such as supervised, unsupervised, semisupervised and reinforcement learning) with differing key parameters, performances as well as advantages/pitfalls in environmental research (Zhu et al., 2023), the rigorous, accurate, robust and also practicable ML analysis requires more research efforts and will be an active and important topic in the future. The ML approach can be a powerful and promising tool to achieve a quantitative closure between the BrC molecules and its total light absorption.

Code availability. The software code to analyze the SP-AMS data is publicly available at: https://cires1.colorado.edu/jimenez-group/ToFAMSResources/ToFSoftware/index.html. The software code to analyze the UPLC-QTOF-MS data is publicly available at: https://systemsomicslab.github.io/compms/msdial/main.html. The software code using SERRF to normalize UPLC-QTOF-MS data is available at: https://slfan.shinyapps.io/ShinySERRF/

Data availability. The data in this study are available from the authors upon request (caxinra@163.com).

Supplement. The supplement related to this article is available online at: XXX

Author contributions. YH, XL and DDH conducted the experiments. YH, XL, RL, BZ, YZ and XG performed the data analysis. YH and XG wrote the paper. All authors reviewed the paper and provide useful suggestions.

Competing interests. The contact author has declared that neither they nor their co-authors have any competing interests.

Disclaimer. Publisher's note: Copernicus Publications remains neutral with regard to jurisdictional claims in published maps and institutional affiliations.

Acknowledgements. We sincerely thank the logistic help from the Center for Experimental Atmospheric Science and Environmental Meteorology of Nanjing University of Information Science and Technology (NUIST) during sampling.

Financial support. This work has been supported by the National Natural Science Foundation of China (grant nos. 22361162668 and 42021004).

914

915 **Review statement.** This paper was edited by XXX, and XXX.

916

917 **References**

918 Aiken, A. C., DeCarlo, P. F., Kroll, J. H., Worsnop, D. R., Huffman, J. A., Docherty,
919 K. h. S., Ulbrich, I. M., Mohr, C., Kimmel, J. l. R., Sueper, D., Sun, Y. l., Zhang, Q.,
920 Trimborn, A., Northway, M., Ziemann, P. J., Canagaratna, M. a. R., Onasch, T. B.,
921 Alfarra, M. R., Prevot, A. S. H., Dommen, J., Duplissy, J., Metzger, A., Baltensperger,
922 U., and Jimenez, J. L.: O/C and OM/OC ratios of primary, secondary, and ambient
923 organic aerosols with high-resolution time-of-flight aerosol mass spectrometry, Environ.
924 Sci. Technol., 42, 4478-4485, https://doi.org/10.1021/es703009q, 2008.

925 Aiona, P. K., Lee, H. J., Leslie, R., Lin, P., Laskin, A., Laskin, J., and Nizkorodov,
926 S. A.: Photochemistry of products of the aqueous reaction of methylglyoxal with
927 ammonium sulfate, ACS Earth Space Chem., 1, 522-532,
928 https://doi.org/10.1021/acsearthspacechem.7b00075, 2017.

929 Al-Abadleh, H. A., Motaghedi, F., Mohammed, W., Rana, M. S., Malek, K. A.,
930 Rastogi, D., Asa-Awuku, A. A., and Guzman, M. I.: Reactivity of aminophenols in
931 forming nitrogen-containing brown carbon from iron-catalyzed reactions, Commun.
932 Chem., 5, 112, https://doi.org/10.1038/s42004-022-00732-1, 2022.

933 Andreae, M. O. and Gelencsér, A.: Black carbon or brown carbon? The nature of
934 light-absorbing carbonaceous aerosols, Atmos. Chem. Phys., 6, 3131-3148,
935 https://doi.org/10.5194/acp-6-3131-2006, 2006.

936 Aurell, J., Gullett, B. K., and Tabor, D.: Emissions from southeastern U.S.
937 Grasslands and pine savannas: Comparison of aerial and ground field measurements
938 with laboratory burns, Atmos. Environ., 111, 170-178,
939 https://doi.org/10.1016/j.atmosenv.2015.03.001, 2015.

940 Bae, E., Yeo, I. J., Jeong, B., Shin, Y., Shin, K. H., and Kim, S.: Study of double
941 bond equivalents and the numbers of carbon and oxygen atom distribution of dissolved
942 organic matter with negative-mode FT-ICR MS, Analytical Chemistry, 83, 4193-4199,

https://doi.org/10.1021/ac200464q, 2011.

Bai, D. P., Wang, H. L., Tan, Y., Yin, Y., Wu, Z. J., Guo, S., Shen, L. J., Zhu, B., Wang, J. H., and Kong, X. C.: Optical properties of aerosols and chemical composition apportionment under different pollution levels in Wuhan during January 2018, https://doi.org/10.3390/atmos11010017, 2020.

Barsotti, F., Ghigo, G., and Vione, D.: Computational assessment of the fluorescence emission of phenol oligomers: A possible insight into the fluorescence properties of humic-like substances (HULIS), J. Photochem. Photobiol., A, 315, 87-93, https://doi.org/10.1016/j.jphotochem.2015.09.012, 2016.

Bhowmik, H. S., Tripathi, S. N., Shukla, A. K., Lalchandani, V., Murari, V., Devaprasad, M., Shivam, A., Bhushan, R., Prévôt, A. S. H., and Rastogi, N.: Contribution of fossil and biomass-derived secondary organic carbon to winter water-soluble organic aerosols in Delhi, India, Sci. Total Environ., 912, 168655, https://doi.org/10.1016/j.scitotenv.2023.168655, 2024.

Birdwell, J. E. and Engel, A. S.: Characterization of dissolved organic matter in cave and spring waters using UV–Vis absorbance and fluorescence spectroscopy, Org. Geochem., 41, 270-280, https://doi.org/10.1016/j.orggeochem.2009.11.002, 2010.

Bond, T. C. and Bergstrom, R. W.: Light absorption by carbonaceous particles: an investigative review, Aerosol Sci. Technol., 40, 27-67, https://doi.org/10.1080/02786820500421521, 2006.

Bones, D. L., Henricksen, D. K., Mang, S. A., Gonsior, M., Bateman, A. P., Nguyen, T. B., Cooper, W. J., and Nizkorodov, S. A.: Appearance of strong absorbers and fluorophores in limonene-O3 secondary organic aerosol due to NH4+-mediated chemical aging over long time scales, J. Geophys. Res.: Atmos., 115, https://doi.org/10.1029/2009JD012864, 2010.

Bozzetti, C., El Haddad, I., Salameh, D., Daellenbach, K. R., Fermo, P., Gonzalez, R., Minguillón, M. C., Iinuma, Y., Poulain, L., Elser, M., Müller, E., Slowik, J. G., Jaffrezo, J. L., Baltensperger, U., Marchand, N., and Prévôt, A. S. H.: Organic aerosol

source apportionment by offline-AMS over a full year in Marseille, Atmos. Chem. Phys., 17, 8247-8268, https://doi.org/10.5194/acp-17-8247-2017, 2017.

Brown, H., Wang, H. L., Flanner, M., Liu, X. H., Singh, B., Zhang, R. D., Yang, Y., and Wu, M. X.: Brown Carbon Fuel and Emission Source Attributions to Global Snow Darkening Effect, J ADV MODEL EARTH SY, 14, https://doi.org/10.1029/2021ms002768, 2022.

Budisulistiorini, S. H., Riva, M., Williams, M., Chen, J., Itoh, M., Surratt, J. D., and Kuwata, M.: Light-absorbing brown carbon aerosol constituents from combustion of indonesian peat and biomass, Environ. Sci. Technol., 51, 4415-4423, https://doi.org/10.1021/acs.est.7b00397, 2017.

Cain, J., Laskin, A., Kholghy, M. R., Thomson, M. J., and Wang, H.: Molecular characterization of organic content of soot along the centerline of a coflow diffusion flame, Phys. Chem. Chem. Phys., 16, 25862-25875, https://doi.org/10.1039/C4CP03330B, 2014.

Canagaratna, M. R., Jayne, J. T., Ghertner, D. A., Herndon, S., Shi, Q., Jimenez, J. L., Silva, P. J., Williams, P., Lanni, T., Drewnick, F., Demerjian, K. L., Kolb, C. E., and Worsnop, D. R.: Chase studies of particulate emissions from in-use New York City vehicles, Aerosol Sci. Technol., 38, 555-573, https://doi.org/10.1080/02786820490465504, 2004.

Canagaratna, M. R., Jimenez, J. L., Kroll, J. H., Chen, Q., Kessler, S. H., Massoli, P., Hildebrandt Ruiz, L., Fortner, E., Williams, L. R., Wilson, K. R., Surratt, J. D., Donahue, N. M., Jayne, J. T., and Worsnop, D. R.: Elemental ratio measurements of organic compounds using aerosol mass spectrometry: characterization, improved calibration, and implications, Atmos. Chem. Phys., 15, 253-272, https://doi.org/10.5194/acp-15-253-2015, 2015.

Cao, T., Li, M. J., Zou, C. L., Fan, X. J., Song, J. Z., Jia, W. L., Yu, C. L., Yu, Z. Q., and Peng, P. A.: Chemical composition, optical properties, and oxidative potential of water- and methanol-soluble organic compounds emitted from the combustion of biomass materials and coal, Atmos. Chem. Phys., 21, 13187-13205,

https://doi.org/10.5194/acp-21-13187-2021, 2021.

Cavalli, F., Facchini, M. C., Decesari, S., Mircea, M., Emblico, L., Fuzzi, S., Ceburnis, D., Yoon, Y. J., O'Dowd, C. D., Putaud, J. P., and Dell'Acqua, A.: Advances in characterization of size-resolved organic matter in marine aerosol over the North Atlantic, J. Geophys. Res.: Atmos., 109, https://doi.org/10.1029/2004JD005137, 2004.

Chakrabarty, R. K., Moosmüller, H., Chen, L. W. A., Lewis, K., Arnott, W. P., Mazzoleni, C., Dubey, M. K., Wold, C. E., Hao, W. M., and Kreidenweis, S. M.: Brown carbon in tar balls from smoldering biomass combustion, Atmos. Chem. Phys., 10, 6363-6370, https://doi.org/10.5194/acp-10-6363-2010, 2010.

Chakrabarty, R. K., Shetty, N. J., Thind, A. S., Beeler, P., Sumlin, B. J., Zhang, C., Liu, P., Idrobo, J. C., Adachi, K., Wagner, N. L., Schwarz, J. P., Ahern, A., Sedlacek, A. J., 3rd, Lambe, A., Daube, C., Lyu, M., Liu, C., Herndon, S., Onasch, T. B., and Mishra, R.: Shortwave absorption by wildfire smoke dominated by dark brown carbon, Nat Geosci, 16, 683-688, https://doi.org/10.1038/s41561-023-01237-9, 2023.

Chen, K. P., Raeofy, N., Lum, M., Mayorga, R., Woods, M., Bahreini, R., Zhang, H. F., and Lin, Y. H.: Solvent effects on chemical composition and optical properties of extracted secondary brown carbon constituents, Aerosol Sci. Technol., 56, 917-930, https://doi.org/10.1080/02786826.2022.2100734, 2022.

Chen, Q. C., Hua, X. Y., Li, J. W., Chang, T., and Wang, Y. Q.: Diurnal evolutions and sources of water-soluble chromophoric aerosols over Xi'an during haze event, in Northwest China, Sci. Total Environ., 786, 147412, https://doi.org/10.1016/j.scitotenv.2021.147412, 2021.

Chen, Q. C., Li, J. W., Hua, X. Y., Jiang, X. T., Mu, Z., Wang, M. M., Wang, J., Shan, M., Yang, X. D., Fan, X. J., Song, J. Z., Wang, Y. Q., Guan, D. J., and Du, L.: Identification of species and sources of atmospheric chromophores by fluorescence excitation-emission matrix with parallel factor analysis, Sci. Total Environ., 718, 137322, https://doi.org/10.1016/j.scitotenv.2020.137322, 2020a.

Chen, Q. C., Miyazaki, Y., Kawamura, K., Matsumoto, K., Coburn, S., Volkamer, R., Iwamoto, Y., Kagami, S., Deng, Y. G., Ogawa, S. H., Ramasamy, S., Kato, S., Ida,

A., Kajii, Y., and Mochida, M.: Characterization of chromophoric water-soluble organic matter in urban, forest, and marine aerosols by HR-ToF-AMS analysis and excitation–emission matrix spectroscopy, Environ. Sci. Technol., 50, 10351-10360, https://doi.org/10.1021/acs.est.6b01643, 2016.

Chen, Y. and Bond, T. C.: Light absorption by organic carbon from wood combustion, Atmos. Chem. Phys., 10, 1773-1787, https://doi.org/10.5194/acp-10-1773-2010, 2010.

Chen, Y. F., Ge, X. L., Chen, H., Xie, X. C., Chen, Y. T., Wang, J. F., Ye, Z. L., Bao, M. Y., Zhang, Y. L., and Chen, M. D.: Seasonal light absorption properties of water-soluble brown carbon in atmospheric fine particles in Nanjing, China, Atmos. Environ., 187, 230-240, https://doi.org/10.1016/j.atmosenv.2018.06.002, 2018.

Chen, Y. F., Xie, X. C., Shi, Z., Li, Y. L., Gai, X. Y., Wang, J. F., Li, H. W., Wu, Y., Zhao, X. Y., Chen, M. D., and Ge, X. L.: Brown carbon in atmospheric fine particles in Yangzhou, China: Light absorption properties and source apportionment, Atmos. Res., 244, 105028, https://doi.org/10.1016/j.atmosres.2020.105028, 2020b.

Cheng, Y., He, K. B., Du, Z. Y., Engling, G., Liu, J. M., Ma, Y. L., Zheng, M., and Weber, R. J.: The characteristics of brown carbon aerosol during winter in Beijing, Atmos. Environ., 127, 355-364, https://doi.org/10.1016/j.atmosenv.2015.12.035, 2016.

Coble, P. G.: Characterization of marine and terrestrial DOM in seawater using excitation-emission matrix spectroscopy, Mar. Chem., 51, 325-346, https://doi.org/10.1016/0304-4203(95)00062-3, 1996.

Daellenbach, K. R., Stefenelli, G., Bozzetti, C., Vlachou, A., Fermo, P., Gonzalez, R., Piazzalunga, A., Colombi, C., Canonaco, F., Hueglin, C., Kasper-Giebl, A., Jaffrezo, J. L., Bianchi, F., Slowik, J. G., Baltensperger, U., El-Haddad, I., and Prévôt, A. S. H.: Long-term chemical analysis and organic aerosol source apportionment at nine sites in central Europe: source identification and uncertainty assessment, Atmos. Chem. Phys., 17, 13265-13282, https://doi.org/10.5194/acp-17-13265-2017, 2017.

DeLessio, M. A., Tsigaridis, K., Bauer, S. E., Chowdhary, J., and Schuster, G. L.: Modeling atmospheric brown carbon in the GISS ModelE Earth system model, Atmos.

Chem. Phys., 24, 6275-6304, https://doi.org/10.5194/acp-24-6275-2024, 2024.

Deng, J. J., Ma, H., Wang, X. F., Zhong, S. J., Zhang, Z. M., Zhu, J. L., Fan, Y. B., Hu, W., Wu, L. B., Li, X. D., Ren, L. J., Pavuluri, C. M., Pan, X. L., Sun, Y. L., Wang, Z. F., Kawamura, K., and Fu, P. Q.: Measurement report: Optical properties and sources of water-soluble brown carbon in Tianjin, North China – insights from organic molecular compositions, Atmos. Chem. Phys., 22, 6449-6470, https://doi.org/10.5194/acp-22-6449-2022, 2022.

Dey, S., Mukherjee, A., Polana, A. J., Rana, A., Mao, J. Y., Jia, S. G., Yadav, A. K., Khillare, P. S., and Sarkar, S.: Brown carbon aerosols in the Indo-Gangetic Plain outflow: insights from excitation emission matrix (EEM) fluorescence spectroscopy, Environ. Sci.: Processes Impacts, 23, 745-755, https://doi.org/10.1039/D1EM00050K, 2021.

Dong, W. M., Wan, J. M., Tokunaga, T. K., Gilbert, B., and Williams, K. H.: Transport and humification of dissolved organic matter within a semi-arid floodplain, J. Environ. Sci, 57, 24-32, https://doi.org/10.1016/j.jes.2016.12.011, 2017.

Dührkop, K., Fleischauer, M., Ludwig, M., Aksenov, A. r. A., Melnik, A. V., Meusel, M., Dorrestein, P. r. C., Rousu, J., and Böcker, S.: SIRIUS 4: a rapid tool for turning tandem mass spectra into metabolite structure information, Nat. Methods, 16, 299-302, https://doi.org/10.1038/s41592-019-0344-8, 2019.

Fan, X. J., Wei, S. Y., Zhu, M. B., Song, J. Z., and Peng, P. A.: Comprehensive characterization of humic-like substances in smoke PM2.5 emitted from the combustion of biomass materials and fossil fuels, Atmos. Chem. Phys., 16, 13321-13340, https://doi.org/10.5194/acp-16-13321-2016, 2016.

Fan, X. J., Yu, X. F., Wang, Y., Xiao, X., Li, F. Y., Xie, Y., Wei, S. Y., Song, J. Z., and Peng, P. A.: The aging behaviors of chromophoric biomass burning brown carbon during dark aqueous hydroxyl radical oxidation processes in laboratory studies, Atmos. Environ., 205, 9-18, https://doi.org/10.1016/j.atmosenv.2019.02.039, 2019.

Fan, Y., Liu, C. Q., Li, L., Ren, L., Ren, H., Zhang, Z., Li, Q., Wang, S., Hu, W., Deng, J., Wu, L., Zhong, S., Zhao, Y., Pavuluri, C. M., Li, X., Pan, X., Sun, Y., Wang,

Z., Kawamura, K., Shi, Z., and Fu, P.: Large contributions of biogenic and anthropogenic sources to fine organic aerosols in Tianjin, North China, Atmos. Chem. Phys., 20, 117-137, https://doi.org/10.5194/acp-20-117-2020, 2020.

Fasola, S., Maio, S., Baldacci, S., La Grutta, S., Ferrante, G., Forastiere, F., Stafoggia, M., Gariazzo, C., and Viegi, G.: Effects of particulate matter on the incidence of respiratory diseases in the pisan longitudinal study, Int. J. Environ. Res. Public Health, 17, https://doi.org/10.3390/ijerph17072540, 2020.

Feng, Y., Ramanathan, V., and Kotamarthi, V. R.: Brown carbon: a significant atmospheric absorber of solar radiation?, Atmos. Chem. Phys., 13, 8607-8621, https://doi.org/10.5194/acp-13-8607-2013, 2013.

Fleming, L. T., Lin, P., Roberts, J. M., Selimovic, V., Yokelson, R., Laskin, J., Laskin, A., and Nizkorodov, S. A.: Molecular composition and photochemical lifetimes of brown carbon chromophores in biomass burning organic aerosol, Atmos. Chem. Phys., 20, 1105-1129, https://doi.org/10.5194/acp-20-1105-2020, 2020.

Fu, P. Q., Kawamura, K., Chen, J., Qin, M. Y., Ren, L. J., Sun, Y. L., Wang, Z. F., Barrie, L. A., Tachibana, E., Ding, A. J., and Yamashita, Y.: Fluorescent water-soluble organic aerosols in the High Arctic atmosphere, Sci. Rep., 5, 9845, https://doi.org/10.1038/srep09845, 2015.

Ge, X. L., Wexler, A. S., and Clegg, S. L.: Atmospheric amines – part I. a review, Atmos. Environ., 45, 524-546, https://doi.org/10.1016/j.atmosenv.2010.10.012, 2011.

Ge, X. L., Sun, Y. L., Trousdell, J., Chen, M. D., and Zhang, Q.: Enhancing characterization of organic nitrogen components in aerosols and droplets using high-resolution aerosol mass spectrometry, Atmos. Meas. Tech., 17, 423-439, https://doi.org/10.5194/amt-17-423-2024, 2024.

Ge, X. L., Li, L., Chen, Y. F., Chen, H., Wu, D., Wang, J. F., Xie, X. C., Ge, S., Ye, Z. L., Xu, J. Z., and Chen, M. D.: Aerosol characteristics and sources in Yangzhou, China resolved by offline aerosol mass spectrometry and other techniques, Environ. Pollut., 225, 74-85, https://doi.org/10.1016/j.envpol.2017.03.044, 2017.

Gilardoni, S., Massoli, P., Paglione, M., Giulianelli, L., Carbone, C., Rinaldi, M.,

Decesari, S., Sandrini, S., Costabile, F., Gobbi, G. P., Pietrogrande, M. C., Visentin, M., Scotto, F., Fuzzi, S., and Facchini, M. C.: Direct observation of aqueous secondary organic aerosol from biomass-burning emissions, Proc. Natl. Acad. Sci. U. S. A., 113, 10013-10018, https://doi.org/10.1073/pnas.1602212113, 2016.

González, C., Mira-M., J., and Juárez, I.: Important variable assessment and electricity price forecasting based on regression tree models: classification and regression trees, Bagging and Random Forests, IET Gener. Transm. Dis., 9, 1120-1128, https://doi.org/10.1049/iet-gtd.2014.0655, 2015.

Gu, C. J., Cui, S. J., Ge, X. L., Wang, Z. Y., Chen, M. J., Qian, Z. H., Liu, Z. Y., Wang, X. F., and Zhang, Y. J.: Chemical composition, sources and optical properties of nitrated aromatic compounds in fine particulate matter during winter foggy days in Nanjing, China, Environ. Res., 212, 113255, https://doi.org/10.1016/j.envres.2022.113255, 2022.

Hawkins, L. N., Lemire, A. N., Galloway, M. M., Corrigan, A. L., Turley, J. J., Espelien, B. M., and De H., D. O.: Maillard chemistry in clouds and aqueous aerosol as a source of atmospheric humic-like substances, Environ. Sci. Technol., 50, 7443-7452, https://doi.org/10.1021/acs.est.6b00909, 2016.

Hecobian, A., Zhang, X., Zheng, M., Frank, N., Edgerton, E. S., and Weber, R. J.: Water-soluble organic aerosol material and the light-absorption characteristics of aqueous extracts measured over the southeastern united states, Atmos. Chem. Phys., 10, 5965-5977, https://doi.org/10.5194/acp-10-5965-2010, 2010.

Hu, J. L., Wang, P., Ying, Q., Zhang, H. L., Chen, J. J., Ge, X. L., Li, X. H., Jiang, J. K., Wang, S. X., Zhang, J., Zhao, Y., and Zhang, Y. Y.: Modeling biogenic and anthropogenic secondary organic aerosol in China, Atmos. Chem. Phys., 17, 77-92, https://doi.org/10.5194/acp-17-77-2017, 2017.

Hu, R. L., Xu, Q. C., Wang, S. X., Hua, Y., Bhattarai, N., Jiang, J K., Song, Y., Daellenbach, K. R., Qi, L., Prevot, A. S. H., and Hao, J. M.: Chemical characteristics and sources of water-soluble organic aerosol in southwest suburb of Beijing, J. Environ. Sci., 95, 99-110, https://doi.org/10.1016/j.jes.2020.04.004, 2020.

Huang, L. B., Liu, T. S., and Grassian, V. i. H.: Radical-Initiated formation of aromatic organosulfates and sulfonates in the aqueous phase, Environ. Sci. Technol., 54, 11857-11864, https://doi.org/10.1021/acs.est.0c05644, 2020.

Huang, R. J., Yang, L., Shen, J. C., Yuan, W., Gong, Y. Q., Ni, H. Y., Duan, J., Yan, J., Huang, H. B., You, Q. H., and Li, Y., J.: Chromophoric fingerprinting of brown carbon from residential biomass burning, Environ. Sci. Technol. Lett., 9, 102-111, https://doi.org/10.1021/acs.estlett.1c00837, 2022.

Huang, R. J., Yang, L., Cao, J. J., Chen, Y., Chen, Q., Li, Y. J., Duan, J., Zhu, C. S., Dai, W. T., Wang, K., Lin, C. S., Ni, H. Y., Corbin, J. C., Wu, Y. F., Zhang, R. J., Tie, X. X., Hoffmann, T., O'Dowd, C., and Dusek, U.: Brown carbon aerosol in urban Xi' an, northwest China: the composition and light absorption properties, Environ. Sci. Technol., 52, 6825-6833, https://doi.org/10.1021/acs.est.8b02386, 2018.

Huguet, A., Vacher, L., Relexans, S., Saubusse, S., Froidefond, J. M., and Parlanti, E.: Properties of fluorescent dissolved organic matter in the Gironde Estuary, Org. Geochem., 40, 706-719, https://doi.org/10.1016/j.orggeochem.2009.03.002, 2009.

Jacobson, M. Z.: Isolating nitrated and aromatic aerosols and nitrated aromatic gases as sources of ultraviolet light absorption, J. Geophys. Res.: Atmos., 104, 3527-3542, https://doi.org/10.1029/1998JD100054, 1999.

Jiang, W. Q., Misovich, M. V., Hettiyadura, A. P. S., Laskin, A., McFall, A. S., Anastasio, C., and Zhang, Q.: Photosensitized Reactions of a phenolic carbonyl from wood combustion in the aqueous phase—chemical evolution and light absorption properties of aqSOA, Environ. Sci. Technol., 55, 5199-5211, https://doi.org/10.1021/acs.est.0c07581, 2021.

Jiang, X. T., Liu, D. T., Li, Q., Tian, P., Wu, Y. Z., Li, S. Y., Hu, K., Ding, S., Bi, K., Li, R. J., Huang, M. Y., Ding, D. P., Chen, Q. C., Kong, S. F., Li, W. J., Pang, Y., and He, D.: Connecting the light absorption of atmospheric organic aerosols with oxidation state and polarity, Environ. Sci. Technol., 56, 12873-12885, https://doi.org/10.1021/acs.est.2c02202, 2022.

Jo, D. S., Park, R. J., Lee, S., Kim, S. W., and Zhang, X.: A global simulation of

brown carbon: implications for photochemistry and direct radiative effect, Atmos. Chem. Phys., 16, 3413-3432, https://doi.org/10.5194/acp-16-3413-2016, 2016.

Kim, H. J., Collier, S., Ge, X. L., Xu, J. Z., Sun, Y. L., Jiang, W. Q., Wang, Y. L., Herckes, P., and Zhang, Q.: Chemical processing of water-soluble species and formation of secondary organic aerosol in fogs, Atmos. Environ., 200, 158-166, https://doi.org/10.1016/j.atmosenv.2018.11.062, 2019.

Kourtchev, I., O'Connor, I. P., Giorio, C., Fuller, S. J., Kristensen, K., Maenhaut, W., Wenger, J. C., Sodeau, J. R., Glasius, M., and Kalberer, M.: Effects of anthropogenic emissions on the molecular composition of urban organic aerosols: An ultrahigh resolution mass spectrometry study, Atmos. Environ., 89, 525-532, https://doi.org/10.1016/j.atmosenv.2014.02.051, 2014.

Kroll, J. H., Donahue, N. M., Jimenez, J. L., Kessler, S. H., Canagaratna, M. R., Wilson, K. R., Altieri, K. E., Mazzoleni, L. R., Wozniak, A. S., Bluhm, H., Mysak, E. R., Smith, J. D., Kolb, C. E., and Worsnop, D. R.: Carbon oxidation state as a metric for describing the chemistry of atmospheric organic aerosol, Nat. Chem., 3, 133-139, https://doi.org/10.1038/nchem.948, 2011.

Kuang, Y., Shang, J., and Chen, Q. C.: Effect of ozone aging on light absorption and fluorescence of brown carbon in soot particles: The important role of polycyclic aromatic hydrocarbons, J. Hazard. Mater., 413, 125406, https://doi.org/10.1016/j.jhazmat.2021.125406, 2021.

Kuang, Y., Shang, J., Sheng, M. S., Shi, X. D., Zhu, J. L., and Qiu, X. H.: Molecular Composition of Beijing PM(2.5) Brown Carbon Revealed by an Untargeted Approach Based on Gas Chromatography and Time-of-Flight Mass Spectrometry, Environ. Sci. Technol., 57, 909-919, https://doi.org/10.1021/acs.est.2c05918, 2023.

Kumar, V., Giannoukos, S., Haslett, S. L., Tong, Y., Singh, A., Bertrand, A., Lee, C. P., Wang, D. S., Bhattu, D., Stefenelli, G., Dave, J. S., Puthussery, J. V., Qi, L., Vats, P., Rai, P., Casotto, R., Satish, R., Mishra, S., Pospisilova, V., Mohr, C., Bell, D. M., Ganguly, D., Verma, V., Rastogi, N., Baltensperger, U., Tripathi, S. N., Prévôt, A. S. H., and Slowik, J. G.: Highly time-resolved chemical speciation and source apportionment

of organic aerosol components in Delhi, India, using extractive electrospray ionization mass spectrometry, Atmos. Chem. Phys., 22, 7739-7761, https://10.5194/acp-22-7739-2022, 2022.

Laskin, A., Laskin, J., and Nizkorodov, S. A.: Chemistry of atmospheric brown carbon, Chem. Rev., 115, 4335-4382, https://doi.org/10.1021/cr5006167, 2015.

Laskin, A., Smith, J. S., and Laskin, J.: Molecular characterization of nitrogen-containing organic compounds in biomass burning aerosols using high-resolution mass spectrometry, Environ. Sci. Technol., 43, 3764-3771, https://doi.org/10.1021/es803456n, 2009.

Laskin, A., West, C. P., and Hettiyadura, A. P. S.: Molecular insights into the composition, sources, and aging of atmospheric brown carbon, Chem Soc Rev, 54, 1583-1612, 10.1039/d3cs00609c, 2025.

Lee, H. L., Laskin, A., Laskin, J., and Nizkorodov, S. A.: Excitation–emission spectra and fluorescence quantum yields for fresh and aged biogenic secondary organic aerosols, Environ. Sci. Technol., 47, 5763-5770, https://doi.org/10.1021/es400644c, 2013.

Lei, R. Y., Sha, Y. Y., Meng, H. F., Huang, Y., Ye, J. H., Huang, D. D., Zhang, Y. J., Wu, Y., Li, Y. J., and Ge, X. L.: Aqueous phase photolysis of 4-nitrocatechol: Reaction kinetics, evolutions of chemical composition, light absorption and oxidation potential, Atmos. Environ., 343, 120981, https://doi.org/10.1016/j.atmosenv.2024.120981, 2025.

Li, H., Qin, X. F., Wang, G. C., Xu, J., Wang, Lu, D., Liu, C., Zheng, H., Liu, J. G., Huang, K., and Deng, C. R.: Conjoint impacts of continental outflows and marine sources on brown carbon in the East China sea: Abundances, optical properties, and formation processes, Atmos. Environ., 273, 118959, https://doi.org/10.1016/j.atmosenv.2022.118959, 2022a.

Li, H. W., Cui, L., Huang, Y., Zhang, Y. J., Wang, J. F., Chen, M. D., and Ge, X. L.: Concurrent dominant pathways of multifunctional products formed from nocturnal isoprene oxidation, Chemosphere, 322, 138185,

https://doi.org/10.1016/j.chemosphere.2023.138185, 2023.

Li, M., Wang, X. F., Lu, C. Y., Li, R., Zhang, J., Dong, S. W., Yang, L. X., Xue, L., Chen, J. M., and Wang, W. X.: Nitrated phenols and the phenolic precursors in the atmosphere in urban Jinan, China, Sci. Total Environ., 714, 136760, https://doi.org/10.1016/j.scitotenv.2020.136760, 2020.

Li, M. J., Fan, X. J., Zhu, M. B., Zou, C. L., Song, J. Z., Wei, S. Y., Jia, W. L., and Peng, P. A.: Abundance and light absorption properties of brown carbon emitted from residential coal combustion in China, Environ. Sci. Technol., 53, 595-603, https://doi.org/10.1021/acs.est.8b05630, 2019.

Li, S., Chen, C., Yang, G.-l., Fang, J., Sun, Y., Tang, L., Wang, H., Xiang, W., Zhang, H., Croteau, P. L., Jayne, J. T., Liao, H., Ge, X., Favez, O., and Zhang, Y.: Sources and processes of organic aerosol in non-refractory PM1 and PM2.5 during foggy and haze episodes in an urban environment of the Yangtze River Delta, China, Environ. Res., 212, 113557, https://doi.org/10.1016/j.envres.2022.113557, 2022b.

Li, X. D., Tao, Y., Zhu, L. W., Ma, S. S., Luo, S. P., Zhao, Z. Z., Sun, N., Ge, X. L., and Ye, Z. L.: Optical and chemical properties and oxidative potential of aqueous-phase products from OH and 3C∗-initiated photooxidation of eugenol, Atmos. Chem. Phys., 22, 7793-7814, https://doi.org/10.5194/acp-22-7793-2022, 2022c.

Lin, G. X., Penner, J. E., Flanner, M. G., Sillman, S., Xu, L., and Zhou, C.: Radiative forcing of organic aerosol in the atmosphere and on snow: effects of SOA and brown carbon, J. Geophys. Res.: Atmos., 119, 7453-7476, https://doi.org/10.1002/2013JD021186, 2014.

Lin, P., Rincon, A. G., Kalberer, M., and Yu, J. Z.: Elemental composition of HULIS in the pearl river delta region, China: results inferred from positive and negative electrospray high resolution mass spectrometric data, Environ. Sci. Technol., 46, 7454-7462, https://doi.org/10.1021/es300285d, 2012.

Lin, P., Fleming, L. T., Nizkorodov, S. A., Laskin, J., and Laskin, A.: Comprehensive molecular characterization of atmospheric brown carbon by high resolution mass spectrometry with electrospray and atmospheric pressure

photoionization, Anal. Chem., 90, 12493-12502, https://doi.org/10.1021/acs.analchem.8b02177, 2018.

Lin, P., Bluvshtein, N., Rudich, Y., Nizkorodov, S. A., Laskin, J., and Laskin, A.: Molecular chemistry of atmospheric brown carbon inferred from a nationwide biomass burning event, Environ. Sci. Technol., 51, 11561-11570, https://doi.org/10.1021/acs.est.7b02276, 2017.

Lin, P., Liu, J. M., Shilling, J. E., Kathmann, S. M., Laskin, J., and Laskin, A.: Molecular characterization of brown carbon (BrC) chromophores in secondary organic aerosol generated from photo-oxidation of toluene, Phys. Chem. Chem. Phys., 17, 23312-23325, https://doi.org/10.1039/C5CP02563J, 2015.

Lin, P., Aiona, P. K., Li, Y., Shiraiwa, M., Laskin, J., Nizkorodov, S. A., and Laskin, A.: Molecular characterization of brown carbon in ciomass curning aerosol particles, Environ. Sci. Technol., 50, 11815-11824, https://doi.org/10.1021/acs.est.6b03024, 2016.

Liu, S. J., Wang, Y. Q., Zhang, S., Chen, Y. B., Wu, C., Zhang, G. Q., and Wang, G. H.: The synergistic effect of NOx and SO2 on the formation and light absorption of secondary organic aerosols from o-xylene photooxidation, Atmos. Res., 304, https://doi.org/10.1016/j.atmosres.2024.107387, 2024.

Liu, Y., Li, H. W., Cui, S. J., Nie, D. Y., Chen, Y. F., and Ge, X. L.: Chemical Characteristics and Sources of Water-Soluble Organic Nitrogen Species in PM2.5 in Nanjing, China, https://doi.org/10.3390/atmos12050574, 2021.

Lobodin, V. V., Marshall, A. G., and Hsu, C. S.: Compositional space boundaries for organic compounds, Analytical Chemistry, 84, 3410-3416, https://doi.org/10.1021/ac300244f, 2012.

Ma, Y. L. and Hays, M. D.: Thermal extraction – two-dimensional gas chromatography–mass spectrometry with heart-cutting for nitrogen heterocyclics in biomass burning aerosols, J. Chromatogr. A, 1200, 228-234, https://doi.org/10.1016/j.chroma.2008.05.078, 2008.

Mao, J. F., Cheng, Y., Bai, Z., Zhang, W., Zhang, L. Y., Chen, H., Wang, L. N., Li, L., and Chen, J. M.: Molecular characterization of nitrogen-containing organic compounds in the winter North China Plain, Sci Total Environ, 838, 156189, https://10.1016/j.scitotenv.2022.156189, 2022.

Matos, J. T. V., Freire, S. M. S. C., Duarte, R. M. B. O., and Duarte, A. C.: Natural organic matter in urban aerosols: comparison between water and alkaline soluble components using excitation–emission matrix fluorescence spectroscopy and multiway data analysis, Atmos. Environ., 102, 1-10, https://doi.org/10.1016/j.atmosenv.2014.11.042, 2015.

McKnight, D. M., Boyer, E. W., Westerhoff, P. K., Doran, P. T., Kulbe, T., and Andersen, D. T.: Spectrofluorometric characterization of dissolved organic matter for indication of precursor organic material and aromaticity, Limnol. Oceanogr., 46, 38-48, https://doi.org/10.4319/lo.2001.46.1.0038, 2001.

McNeill, V. F.: Aqueous organic chemistry in the atmosphere: sources and chemical processing of organic aerosols, Environ. Sci. Technol., 49, 1237-1244, https://doi.org/10.1021/es5043707, 2015.

Murphy, K. R., Stedmon, C. A., Graeber, D., and Bro, R.: Fluorescence spectroscopy and multi-way techniques. PARAFAC, Anal. Methods, 5, https://doi.org/10.1039/c3ay41160e, 2013.

Murphy, K. R., Hambly, A., Singh, S., Henderson, R. K., Baker, A., Stuetz, R., and Khan, S. J.: Organic matter fluorescence in municipal water recycling schemes: toward a unified PARAFAC model, Environ. Sci. Technol., 45, 2909-2916, https://doi.org/10.1021/es103015e, 2011.

Negron-Encarnacion, I. and Arce, R.: Light-induced transformations of aza-aromatic pollutants adsorbed on models of atmospheric particulate matter: Acridine and 9(10-H) acridone, Atmos. Environ., 41, 6771-6783, https://doi.org/10.1016/j.atmosenv.2007.04.062, 2007.

O'Brien, R. E., Ridley, K. J., Canagaratna, M. R., Jayne, J. T., Croteau, P. L., Worsnop, D. R., Budisulistiorini, S. H., Surratt, J. D., Follett, C. L., Repeta, D. J., and

Kroll, J. H.: Ultrasonic nebulization for the elemental analysis of microgram-level samples with offline aerosol mass spectrometry, Atmos. Meas. Tech., 12, 1659-1671, https://doi.org/10.5194/amt-12-1659-2019, 2019.

Onasch, T. B., Trimborn, A., Fortner, E. C., Jayne, J. T., Kok, G. L., Williams, L. R., Davidovits, P., and Worsnop, D. R.: Soot particle aerosol mass spectrometer: development, validation, and initial application, Aerosol Sci. Technol., 46, 804-817, https://doi.org/10.1080/02786826.2012.663948, 2012.

Ou, Y., Nie, D. Y., Chen, H., Ye, Z. L., and Ge, X. L.: Characterization of products from the aqueous-phase photochemical oxidation of benzene-diols, Atmosphere, 12, https://doi.org/10.3390/atmos12050534, 2021.

Petters, S. S., Cui, T. Q., Zhang, Z. F., Gold, A., McNeill, V. F., Surratt, J. D., and Turpin, B. J.: Organosulfates from dark aqueous reactions of isoprene-derived epoxydiols under cloud and fog conditions: kinetics, mechanism, and effect of reaction environment on regioselectivity of sulfate addition, ACS Earth Space Chem., 5, 474-486, https://doi.org/10.1021/acsearthspacechem.0c00293, 2021.

Powelson, M. H., Espelien, B. M., Hawkins, L. N., Galloway, M. M., and De Haan, D. O.: Brown Carbon Formation by Aqueous-Phase Carbonyl Compound Reactions with Amines and Ammonium Sulfate, Environ. Sci. Technol., 48, 985-993, https://doi.org/10.1021/es4038325, 2014.

Qi, L., Chen, M. D., Stefenelli, G., Pospisilova, V., Tong, Y. D., Bertrand, A., Hueglin, C., Ge, X. L., Baltensperger, U., Prévôt, A. S. H., and Slowik, J. G.: Organic aerosol source apportionment in Zurich using an extractive electrospray ionization time-of-flight mass spectrometer (EESI-TOF-MS) – Part 2: biomass burning influences in winter, Atmos. Chem. Phys., 19, 8037-8062, https://doi.org/10.5194/acp-19-8037-2019, 2019.

Qin, J. J., Zhang, L. M., Zhou, X. M., Duan, J. C., Mu, S. T., Xiao, K., Hu, J. N., and Tan, J. H.: Fluorescence fingerprinting properties for exploring water-soluble organic compounds in PM2.5 in an industrial city of northwest China, Atmos. Environ., 184, 203-211, https://doi.org/10.1016/j.atmosenv.2018.04.049, 2018.

Qin, Y. M., Tan, H. B., Li, Y. J., Schurman, M. I., Li, F., Canonaco, F., Prévôt, A. S. H., and Chan, C. K.: Impacts of traffic emissions on atmospheric particulate nitrate and organics at a downwind site on the periphery of Guangzhou, China, Atmos. Chem. Phys., 17, 10245-10258, https://doi.org/10.5194/acp-17-10245-2017, 2017.

Qiu, Y. M., Xie, Q. R., Wang, J. F., Xu, W. Q., Li, L. J., Wang, Q. Q., Zhao, J., Chen, Y. T., Chen, Y. F., Wu, Y. Z., Du, W., Zhou, W., Lee, J., Zhao, C. F., Ge, X. L., Fu, P. Q., Wang, Z., Worsnop, D. R., and Sun, Y. L.: Vertical characterization and source apportionment of water-soluble organic aerosol with high-resolution aerosol mass spectrometry in Beijing, China, ACS Earth Space Chem., 3, 273-284, https://doi.org/10.1021/acsearthspacechem.8b00155, 2019.

Shapiro, E. L., Szprengiel, J., Sareen, N., Jen, C. N., Giordano, M. R., and McNeill, V. F.: Light-absorbing secondary organic material formed by glyoxal in aqueous aerosol mimics, Atmos. Chem. Phys., 9, 2289-2300, https://doi.org/10.5194/acp-9-2289-2009, 2009.

Song, J. Z., Li, M. J., Fan, X. J., Zou, C. L., Zhu, M. B., Jiang, B., Yu, Z. Q., Jia, W. L., Liao, Y. H., and Peng, P. A.: Molecular Characterization of water- and methanol-soluble organic compounds emitted from residential coal combustion using ultrahigh-resolution electrospray ionization fourier transform ion cyclotron resonance mass spectrometry, Environ. Sci. Technol., 53, 13607-13617, https://doi.org/10.1021/acs.est.9b04331, 2019.

Stubbins, A., Lapierre, J. F., Berggren, M., Prairie, Y. T., Dittmar, T., and del Giorgio, P. A.: What's in an EEM? Molecular Signatures Associated with Dissolved Organic Fluorescence in Boreal Canada, Environ. Sci. Technol., 48, 10598-10606, https://doi.org/10.1021/es502086e, 2014.

Sun, Y. L., Du, W., Fu, P. Q., Wang, Q. Q., Li, J., Ge, X. L., Zhang, Q., Zhu, C. M., Ren, L. J., Xu, W. Q., Zhao, J., Han, T. T., Worsnop, D. R., and Wang, Z.: Primary and secondary aerosols in Beijing in winter: sources, variations and processes, Atmos. Chem. Phys., 16, 8309-8329, https://doi.org/10.5194/acp-16-8309-2016, 2016.

Tang, J., Li, J., Su, T., Han, Y., Mo, Y. Z., Jiang, H. X., Cui, M., Jiang, B., Chen,

Y. J., Tang, J. H., Song, J. Z., Peng, P. A., and Zhang, G.: Molecular compositions and optical properties of dissolved brown carbon in biomass burning, coal combustion, and vehicle emission aerosols illuminated by excitation–emission matrix spectroscopy and Fourier transform ion cyclotron resonance mass spectrometry analysis, Atmos. Chem. Phys., 20, 2513-2532, https://doi.org/10.5194/acp-20-2513-2020, 2020.

Tang, J., Li, J., Zhao, S. Z., Zhong, G. C., Mo, Y. Z., Jiang, H. X., Jiang, B., Chen, Y. J., Tang, J. H., Tian, C. G., Zong, Z., Hussain S., J., Song, J. Z., and Zhang, G.: Molecular signatures and formation mechanisms of water-soluble chromophores in particulate matter from Karachi in Pakistan, Sci. Total Environ., 914, 169890, https://doi.org/10.1016/j.scitotenv.2024.169890, 2024.

Tsugawa, H., Cajka, T., Kind, T., Ma, Y., Higgins, B., Ikeda, K., Kanazawa, M., VanderGheynst, J., Fiehn, O., and Arita, M.: MS-DIAL: data-independent MS/MS deconvolution for comprehensive metabolome analysis, Nat. Methods, 12, 523-526, https://doi.org/10.1038/nmeth.3393, 2015.

Ulbrich, I. M., Canagaratna, M. R., Zhang, Q., Worsnop, D. R., and Jimenez, J. L.: Interpretation of organic components from Positive Matrix Factorization of aerosol mass spectrometric data, Atmos. Chem. Phys., 9, 2891-2918, https://doi.org/10.5194/acp-9-2891-2009, 2009.

Updyke, K. M., Nguyen, T. B., and Nizkorodov, S. A.: Formation of brown carbon via reactions of ammonia with secondary organic aerosols from biogenic and anthropogenic precursors, Atmos. Environ., 63, 22-31, https://doi.org/10.1016/j.atmosenv.2012.09.012, 2012.

Vasilakopoulou, C. N., Florou, K., Kaltsonoudis, C., Stavroulas, I., Mihalopoulos, N., and Pandis, S. N.: Development and evaluation of an improved offline aerosol mass spectrometry technique, Atmos. Meas. Tech., 16, 2837-2850, https://doi.org/10.5194/amt-16-2837-2023, 2023.

Veld, M., Khare, P., Hao, Y. F., Reche, C., Pérez, N., Alastuey, A., Yus-Díez, J., Marchand, N., Prevot, A. S. H., Querol, X., and Daellenbach, K. R.: Characterizing the sources of ambient PM10 organic aerosol in urban and rural Catalonia, Spain, Sci. Total

Environ., 902, 166440, https://doi.org/10.1016/j.scitotenv.2023.166440, 2023.

Wang, D. W., Shen, Z. X., Zhang, Q., Lei, Y. L., Zhang, T., Huang, S. S., Sun, J., Xu, H. M., and Cao, J. J.: Winter brown carbon over six of China's megacities: light absorption, molecular characterization, and improved source apportionment revealed by multilayer perceptron neural network, Atmos. Chem. Phys., 22, 14893-14904, https://doi.org/10.5194/acp-22-14893-2022, 2022a.

Wang, J. F., Ge, X. L., Sonya, C., Ye, J. H., Lei, Y. L., Chen, M. D., and Zhang, Q.: Influence of regional emission controls on the chemical composition, sources, and size distributions of submicron aerosols: Insights from the 2014 Nanjing Youth Olympic Games, Sci. Total Environ., 807, 150869, https://doi.org/10.1016/j.scitotenv.2021.150869, 2022b.

Wang, J. F., Ge, X. L., Chen, Y. F., Shen, Y. F., Zhang, Q., Sun, Y. L., Xu, J. Z., Ge, S., Yu, H., and Chen, M. D.: Highly time-resolved urban aerosol characteristics during springtime in Yangtze River Delta, China: insights from soot particle aerosol mass spectrometry, Atmos. Chem. Phys., 16, 9109-9127, https://doi.org/10.5194/acp-16-9109-2016, 2016.

Wang, J. F., Ye, J. H., Zhang, Q., Zhao, J., Wu, Y. Z., Li, J. Y., Liu, D. T., Li, W. J., Zhang, Y. G., Wu, C., Xie, C. H., Qin, Y. M., Lei, Y. L., Huang, X. P., Guo, J. P., Liu, P. F., Fu, P. Q., Li, Y. J., Lee, H. C., Choi, H., Zhang, J., Liao, H., Chen, M. D., Sun, Y. L., Ge, X. L., Martin, S. T., and Jacob, D. J.: Aqueous production of secondary organic aerosol from fossil-fuel emissions in winter Beijing haze, Proc. Natl. Acad. Sci. U. S. A., 118, https://doi.org/10.1073/pnas.2022179118, 2021.

Wang, K., Zhang, Y., Huang, R. J., Cao, J. J., and Hoffmann, T.: UHPLC-Orbitrap mass spectrometric characterization of organic aerosol from a central European city (Mainz, Germany) and a Chinese megacity (Beijing), Atmos. Environ., 189, 22-29, https://doi.org/10.1016/j.atmosenv.2018.06.036, 2018a.

Wang, L. W., Wang, X. F., Gu, R. R., Wang, H., Yao, L., Wen, L., Zhu, F. P., Wang, W. H., Xue, L. K., Yang, L. X., Lu, K. D., Chen, J. M., Wang, T., Zhang, Y. H., and Wang, W. X.: Observations of fine particulate nitrated phenols in four sites in northern

China: concentrations, source apportionment, and secondary formation, Atmos. Chem. Phys., 18, 4349-4359, https://doi.org/10.5194/acp-18-4349-2018, 2018b.

Wang, Y., Huang, R. J., Zhong, H. B., Wang, T., Yang, L., Yuan, W., Xu, W., and An, Z. S.: Predictions of the Optical Properties of Brown Carbon Aerosol by Machine Learning with Typical Chromophores, Environ. Sci. Technol., 58, 20588-20597, https://doi.org/10.1021/acs.est.4c09031, 2024.

Wang, Y. J., Hu, M., Lin, P., Guo, Q. F., Wu, Z. J., Li, M. G., Zeng, L. M., Song, Y., Zeng, L. W., Wu, Y. S., Guo, S., Huang, X. F., and He, L. Y.: Molecular characterization of nitrogen-containing organic compounds in humic-like substances emitted from straw residue burning, Environ. Sci. Technol., 51, 5951-5961, https://doi.org/10.1021/acs.est.7b00248, 2017.

Wang, Y. Q.: An open source software suite for multi-dimensional meteorological data computation and visualisation, Journal of Open Research Software, 7, https://doi.org/10.5334/jors.267, 2019.

Wen, H., Zhou, Y., Xu, X. Y., Wang, T. S., Chen, Q. L., Chen, Q. C., Li, W. J., Wang, Z., Huang, Z. W., Zhou, T., Shi, J. S., Bi, J. R., Ji, M. X., and Wang, X.: Water-soluble brown carbon in atmospheric aerosols along the transport pathway of Asian dust: Optical properties, chemical compositions, and potential sources, Sci. Total Environ., 789, 147971, https://doi.org/10.1016/j.scitotenv.2021.147971, 2021.

Wu, G. M., Ram, K., Fu, P. Q., Wang, W., Zhang, Y. L., Liu, X. Y., Stone, E. A., Pradhan, B. B., Dangol, P. M., Panday, A. K., Wan, X., Bai, Z. P., Kang, S. C., Zhang, Q. G., and Cong, Z. Y.: Water-soluble brown carbon in atmospheric aerosols from Godavari (Nepal), a regional representative of south Asia, Environ. Sci. Technol., 53, 3471-3479, https://doi.org/10.1021/acs.est.9b00596, 2019a.

Wu, Y. Z., Ge, X. L., Wang, J. F., Shen, Y. F., Ye, Z. L., Ge, S., Wu, Y., Yu, H., and Chen, M. D.: Responses of secondary aerosols to relative humidity and photochemical activities in an industrialized environment during late winter, Atmos. Environ., 193, 66-78, https://doi.org/10.1016/j.atmosenv.2018.09.008, 2018.

Wu, Y. Z., Liu, D. T., Wang, J. F., Shen, F. Z., Chen, Y. F., Cui, S. J., Ge, S., Wu,

Y., Chen, M. D., and Ge, X. L.: Characterization of size-resolved hygroscopicity of black carbon-containing particle in urban environment, Environ. Sci. Technol., 53, 14212-14221, https://doi.org/10.1021/acs.est.9b05546, 2019b.

Xian, J. K., Cui, S. J., Chen, X. Z., Wang, J. Y., Xiong, Y. F., Gu, C. J., Wang, Y., Zhang, Y. J., Li, H. W., Wang, J. F., and Ge, X. L.: Online chemical characterization of atmospheric fine secondary aerosols and organic nitrates in summer Nanjing, China, Atmos. Res., 290, 106783, https://doi.org/10.1016/j.atmosres.2023.106783, 2023.

Xie, M. J., Mladenov, N., Williams, M. W., Neff, J. C., Wasswa, J., and Hannigan, M. P.: Water soluble organic aerosols in the Colorado Rocky Mountains, USA: composition, sources and optical properties, Sci. Rep., 6, 39339, https://doi.org/10.1038/srep39339, 2016.

Xie, X. C., Chen, Y. F., Nie, D. Y., Liu, Y., Liu, Y., Lei, R. Y., Zhao, X. Y., Li, H. W., and Ge, X. L.: Light-absorbing and fluorescent properties of atmospheric brown carbon: A case study in Nanjing, China, Chemosphere, 251, 126350, https://doi.org/10.1016/j.chemosphere.2020.126350, 2020.

Xing, C., Wan, Y. B., Wang, Q. Q., Kong, S. F., Huang, X. P., Ge, X. L., Xie, M. J., and Yu, H.: Molecular Characterization of Brown Carbon Chromophores in Atmospherically Relevant Samples and Their Gas-Particle Distribution and Diurnal Variation in the Atmosphere, J. Geophys. Res.: Atmos., 128, e2022JD038142, https://doi.org/10.1029/2022JD038142, 2023.

Xu, L. L., Lin, G. X., Liu, X. H., Wu, C. L., Wu, Y. F., and Lou, S. J.: Constraining Light Absorption of Brown Carbon in China and Implications for Aerosol Direct Radiative Effect, Geophys. Res. Lett., 51, https://doi.org/10.1029/2024gl109861, 2024.

Yan, G. and Kim, G.: Speciation and sources of brown carbon in precipitation at seoul, Korea: insights from excitation–emission matrix spectroscopy and carbon isotopic analysis, Environ. Sci. Technol., 51, 11580-11587, https://doi.org/10.1021/acs.est.7b02892, 2017.

Yan, J. P., Wang, X. P., Gong, P., Wang, C. F., and Cong, Z. Y.: Review of brown carbon aerosols: recent progress and perspectives, Sci. Total Environ., 634, 1475-1485,

https://doi.org/10.1016/j.scitotenv.2018.04.083, 2018.

Yassine, M. M., Harir, M., Dabek-Z., E., and Schmitt-K., P.: Structural characterization of organic aerosol using Fourier transform ion cyclotron resonance mass spectrometry: Aromaticity equivalent approach, Rapid Commun. Mass Spectrom., 28, 2445-2454, https://doi.org/doi.org/10.1002/rcm.7038, 2014.

Ye, Z. L., Qu, Z. X., Ma, S. S., Luo, S. P., Chen, Y. T., Chen, H., Chen, Y. F., Zhao, Z. Z., Chen, M. D., and Ge, X. L.: A comprehensive investigation of aqueous-phase photochemical oxidation of 4-ethylphenol, Sci. Total Environ., 685, 976-985, https://doi.org/10.1016/j.scitotenv.2019.06.276, 2019.

Ye, Z. L., Li, Q., Liu, J. S., Luo, S. P., Zhou, Q. F., Bi, C. L., Ma, S. S., Chen, Y. F., Chen, H., Li, L., and Ge, X. L.: Investigation of submicron aerosol characteristics in Changzhou, China: Composition, source, and comparison with co-collected PM2.5, Chemosphere, 183, 176-185, https://doi.org/10.1016/j.chemosphere.2017.05.094, 2017.

Yu, H. R., Liang, H., Qu, F. S., Han, Z. S., Shao, S. L., Chang, H. Q., and Li, G. B.: Impact of dataset diversity on accuracy and sensitivity of parallel factor analysis model of dissolved organic matter fluorescence excitation-emission matrix, Sci. Rep., 5, 10207, https://doi.org/10.1038/srep10207, 2015.

Yu, J. T., Yan, C. Q., Liu, Y., Li, X. Y., Zhou, T., and Zheng, M.: Potassium: a tracer for biomass burning in Beijing?, Aerosol Air Qual. Res., 18, 2447-2459, https://doi.org/10.4209/aaqr.2017.11.0536, 2018.

Zhang, B. Q., Zhang, Y. J., Zhang, K. X., Zhang, Y. C., Ji, Y., Zhu, B. Z., Liang, Z. Y., Wang, H. L., and Ge, X. L.: Machine learning assesses drivers of PM2.5 air pollution trend in the Tibetan Plateau from 2015 to 2022, Sci. Total Environ., 878, 163189, https://doi.org/10.1016/j.scitotenv.2023.163189, 2023.

Zhang, Q., Jimenez, J. L., Canagaratna, M. R., Ulbrich, I. M., Ng, N. L., Worsnop, D. s. R., and Sun, Y. L.: Understanding atmospheric organic aerosols via factor analysis of aerosol mass spectrometry: a review, Anal. Bioanal. Chem., 401, 3045-3067, https://doi.org/10.1007/s00216-011-5355-y, 2011.

Zhang, S. Y.: Detection of scopolamine in nori fruit juice and its traditional chinese

medicine compound health products by high performance liquid chromatography, World Latest Medicine Information, 18, 91-92, https://doi.org/10.19613/j.cnki.1671-3141.2018.82.066, 2018.

Zhang, X. L., Lin, Y. H., Surratt, J. D., and Weber, R. J.: Sources, composition and absorption Ångström exponent of light-absorbing organic components in aerosol extracts from the Los Angeles basin, Environ. Sci. Technol., 47, 3685-3693, https://doi.org/10.1021/es305047b, 2013.

Zhang, Y. Z., Forrister, H., Liu, J. M., Dibb, J., Anderson, B., Schwarz, J. P., Perring, A. E., Jimenez, J. L., Campuzano-Jost, P., Wang, Y. H., Nenes, A., and Weber, R. J.: Top-of-atmosphere radiative forcing affected by brown carbon in the upper troposphere, Nat. Geosci., 10, 486-489, https://doi.org/10.1038/ngeo2960, 2017.

Zhao, R., Lee, A. K. Y., Huang, L., Li, X., Yang, F., and Abbatt, J. P. D.: Photochemical processing of aqueous atmospheric brown carbon, Atmos. Chem. Phys., 15, 6087-6100, https://doi.org/10.5194/acp-15-6087-2015, 2015.

Zhong, M., Xu, J. Z., Wang, H. Q., Gao, L., Zhu, H. X., Zhai, L. X., Zhang, X. H., and Zhao, W. H.: Characterizing water-soluble brown carbon in fine particles in four typical cities in northwestern China during wintertime: integrating optical properties with chemical processes, Atmos. Chem. Phys., 23, 12609-12630, https://doi.org/10.5194/acp-23-12609-2023, 2023.

Zhu, B., Fang, J., Zhang, Y., Qiu, J., Chen, K., Zhang, K., Liang, H., Yang, H., Ding, Y., and Ge, X.: Machine learning elucidates ubiquity of enhanced ozone air pollution in China linked to the spring festival effect, Atmos. Pollut. Res., 15, 102127, https://doi.org/10.1016/j.apr.2024.102127, 2024.

Zhu, J. J., Yang, M., and Ren, Z. J.: Machine Learning in Environmental Research: Common Pitfalls and Best Practices, Environ Sci Technol, 57, 17671-17689, https://doi.org/10.1021/acs.est.3c00026, 2023.

Zorn, S. R., Drewnick, F., Schott, M., Hoffmann, T., and Borrmann, S.: Characterization of the South Atlantic marine boundary layer aerosol using an aerodyne aerosol mass spectrometer, Atmos. Chem. Phys., 8, 4711-4728,

https://doi.org/10.5194/acp-8-4711-2008, 2008.

Zsolnay, A., Baigar, E., Jimenez, M., Steinweg, B., and Saccomandi, F.: Differentiating with fluorescence spectroscopy the sources of dissolved organic matter in soils subjected to drying, Chemosphere, 38, 45-50, https://doi.org/10.1016/S0045-6535(98)00166-0, 1999.

1556 Table 1. The average mass concentrations of major chemical components as well as the

1557 parameters of optical properties of $PM_{2.5}$ collected in Nanjing during two seasons.

	Summer Season (SS)			Cold Season (CS)		
	Daytime	Nighttime	Average	Daytime	Nighttime	Average
OC (μg m^{-3})	7.02±3.04	6.87±2.51	6.94±2.76	12.9±5.77	12.74±5.29	12.82±5.51
EC (μg m^{-3})	1.13±0.31	1.22±0.37	1.17±0.34	1.94±0.93	1.6±0.74	1.77±0.86
AAE_{WSOC}	6.34±0.65	6.35±0.69	6.35±0.67	6.43±0.68	6.44±0.86	6.43±0.77
AAE_{MSOC}	6.02±0.90	5.96±0.96	5.99±0.92	7.06±0.94	6.70±0.65	6.89±0.82
WSOC (μg m^{-3})	4.06±1.31	4.45±1.44	4.26±1.38	5.81±2.29	5.75±2.25	6.34±2.27
MSOC (μg m^{-3})	5.64±2.12	5.79±1.89	5.72±1.99	10.42±4.98	10.49±4.57	10.45±4.75
Total ions (μg m^{-3})	18.00±5.49	18.69±8.05	18.49±6.91	35.41±15.02	43.12±17.94	39.22±16.88
$Abs_{365, WSOC}$ (M m^{-1})	2.15±0.90	2.38±0.80	2.27±0.85	4.89±2.63	4.86±2.46	4.87±2.53
$Abs_{365, MSOC}$ (M m^{-1})	3.44±1.40	3.82±1.55	3.64±1.48	4.65±2.24	5.31±2.71	4.97±2.49
$MAE_{365, WSOC}$ (m^2 g^{-1})	0.54±0.16	0.56±0.15	0.55±0.16	0.73±0.20	0.77±0.21	0.75±0.21
$MAE_{365, MSOC}$ (m^2 g^{-1})	0.68±0.32	0.75±0.30	0.72±0.31	0.48±0.18	0.52±0.16	0.50±0.17
SFE_{WSOC}(W g^{-1})	2.16±1.29	2.24±1.36	2.20±1.33	3.16±1.8	3.42±1.25	3.24±1.84
SFE_{MSOC}(W g^{-1})	2.28±2.37	2.55±1.85	2.43±2.10	2.19±1.01	2.26±0.81	2.23±0.91

1558

1559 Table 2. Multi-linear regression results of the four factors and corresponding average
1560 contributions to the total light absorption of water-soluble organics (WSOA).

Factor	Regression Coefficient($m^2 \cdot g^{-1}$)		Contribution (%)
	Average	Standard Error	
HOA	0.71	0.11	33.05
BBOA	0.71	0.06	15.49
OOA1	0.12	0.07	6.00
OOA2	0.83	0.14	45.46

1561

1562 Table 3. The average values of fluorescence indices of both water-soluble organic
1563 carbon (WSOC) and methanol-soluble organic carbon (MSOC).

	Summer Season (SS)			Cold Season (CS)		
	Day	Night	Average	Day	Night	Average
HIX_{WSOC}	3.16±0.74	3.51±1.12	3.34±0.97	4.68±0.94	4.67±0.91	4.68±0.92
HIX_{MSOC}	2.65±0.99	2.78±0.86	2.72±0.92	3.42±0.73	3.53±0.58	3.48±0.66
FI_{WSOC}	1.85±0.16	1.97±0.17	1.91±0.18	1.89±0.11	1.92±0.09	1.90±0.10
FI_{MSOC}	2.25±0.26	2.30±0.31	2.27±0.28	2.10±0.15	2.12±0.14	2.11±0.15
BIX_{WSOC}	0.81±0.16	0.86±0.14	0.84±0.15	0.86±0.10	0.91±0.08	0.88±0.09
BIX_{MSOC}	0.89±0.19	0.9±0.13	0.90±0.16	0.95±0.10	0.97±0.11	0.96±0.10

1564

1565 Table 4. The number percentages of organosulfates (OSs) in CHOS compounds in ESI^-

1566 mode and those of nitrooxy-OSs in CHONS compounds in both modes.

	SS		CS	
	Daytime	Nighttime	Daytime	Nighttime
OSs (ESI^-)	34.8%	42.3%	54.3%	68.6%
Nitrooxy-OSs (ESI^-)	5.3%	12.0%	11.0%	12.5%
Nitrooxy-OSs (ESI^+)	10.3%	11.8%	10.5%	9.8%

1567

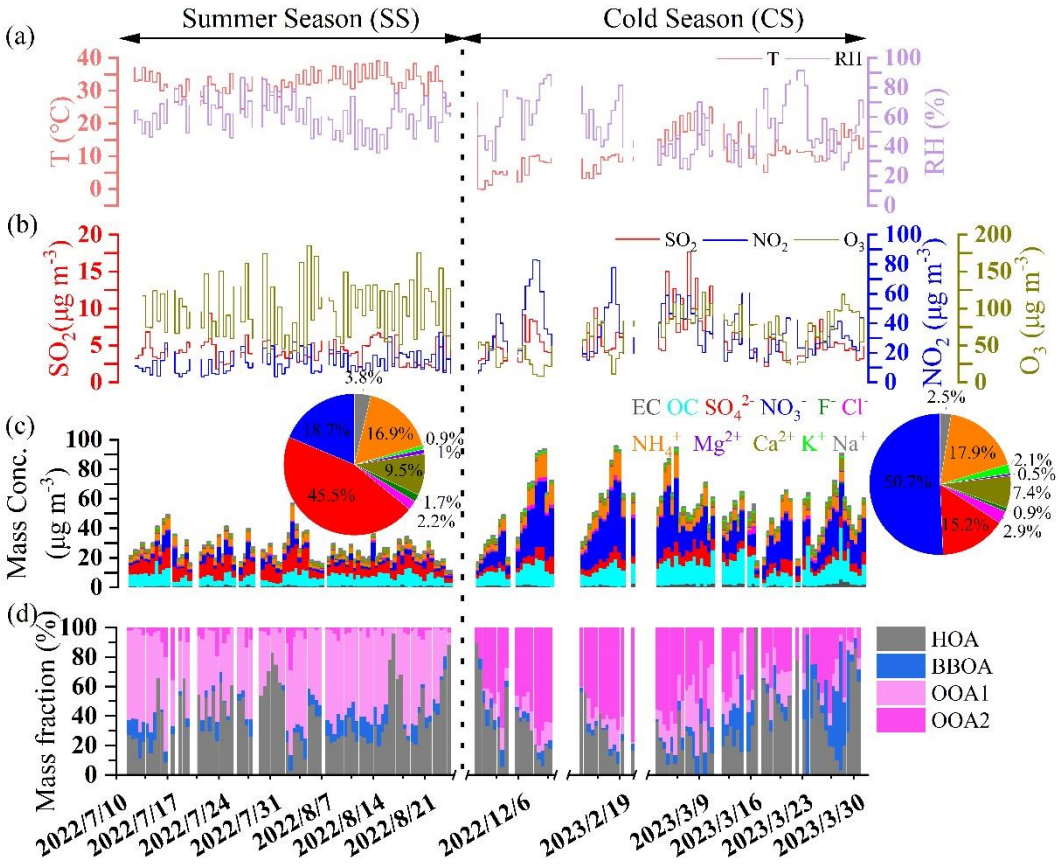

Figure 1. Time series of: (a) air temperature (T) and relative humidity (RH); (b) concentrations of nitrogen dioxide (NO_2), sulfur dioxide (SO_2) and ozone (O_3); (c) concentrations of different inorganic ions, total organic carbon (OC), and elemental carbon (EC) (two inset pies are the average mass contributions of difference ions to the total ions during SS and CS, respectively); and (d) mass percentages of different factors with respect to the total water-soluble OA

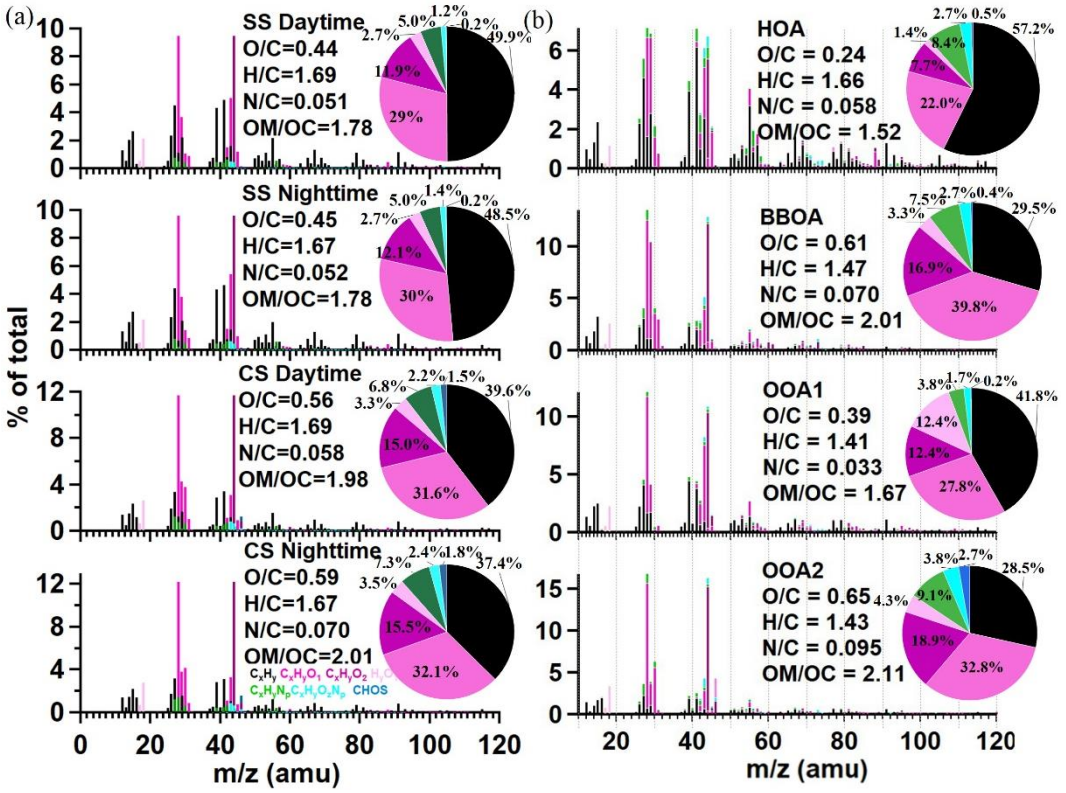

Figure 2. High-resolution mass spectra (HRMS) of (a) the water-soluble OA (WSOA) during different periods, and (b) the four resolved factors (HOA, BBOA, OOA1, OOA2). Ions are classified into and colored by different ion families, and inset pies in both charts show the mass fractional contributions of different ion families to the total HRMS correspondingly.

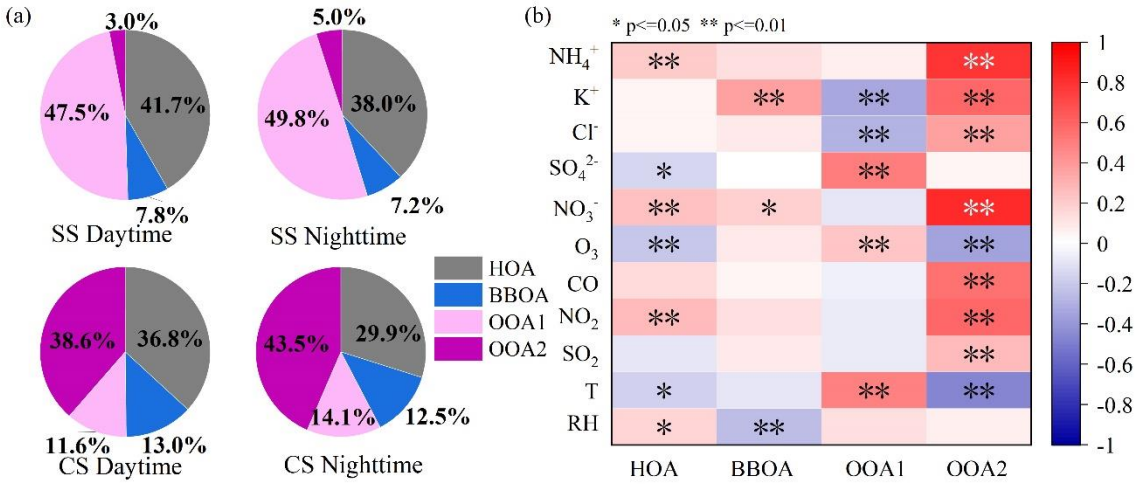

Figure 3. (a) Average mass contributions of the four factor to WSOA during different periods, and (b) cross-correlation coefficients (Pearson's *r*) among the four factors and other aerosol components as well as gaseous species.

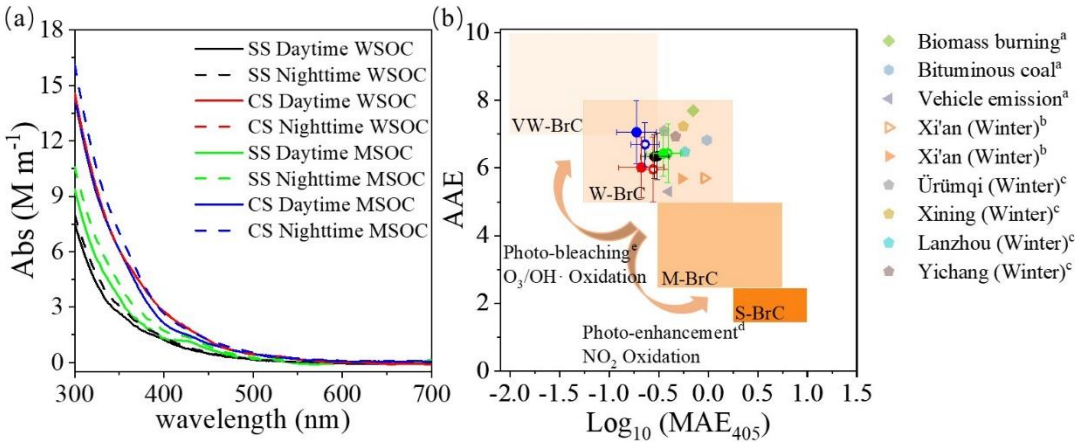

Figure 4. (a) Light absorption coefficients (Abs) of the water-soluble OC (WSOC) and methanol-soluble OC (MSOC) as a function of wavelength, and (b) distribution of the measured data in the $\log_{10}(MAE_{405})$-AAE space (Saleh, 2020)(MAE_{405}: Mass absorption efficiency at 405 nm; AAE: Absorption Ångström Exponent; The shaded areas indicate very weakly (VW), weakly (W), moderately (M), and strongly (S) absorbing brown carbon (BrC), respectively; Other markers indicate results from [a] Huang et al. (2018), [b] Chen et al. (2018) and [c] Zhong et al. (2023).

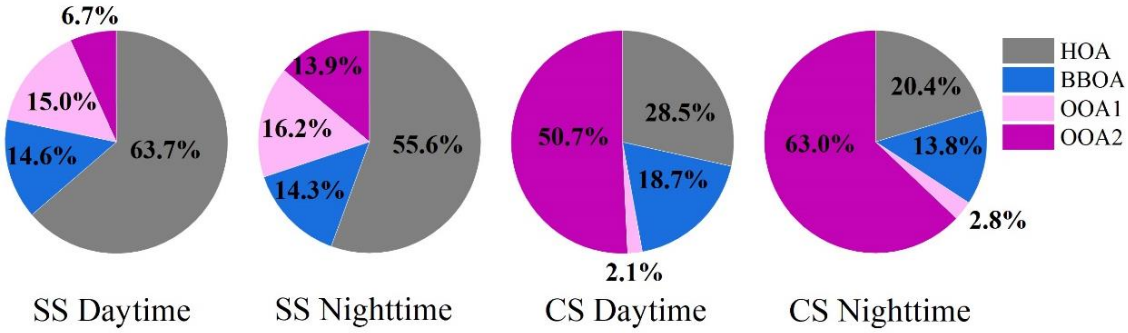

Figure 5. Contributions of the four factors to the total light absorption of WSOA during different periods.

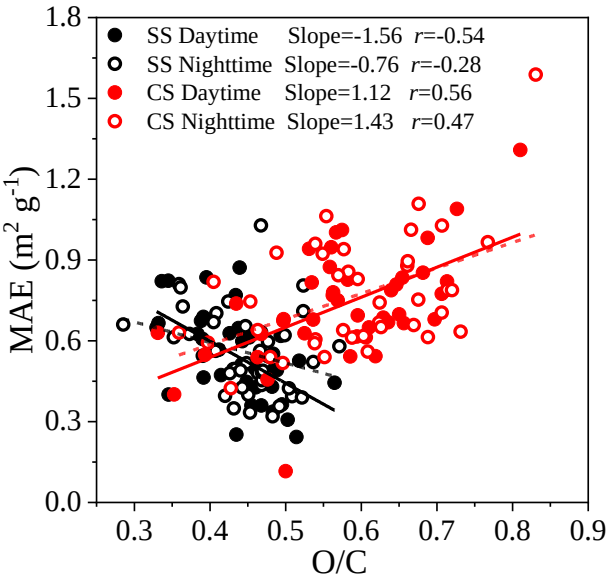

1601

1602 Figure 6. Scatter plot of MAE_{365} (mass absorption efficiency at 365 nm) versus the

1603 oxygen-to-carbon (O/C) ratios for the WSOA.

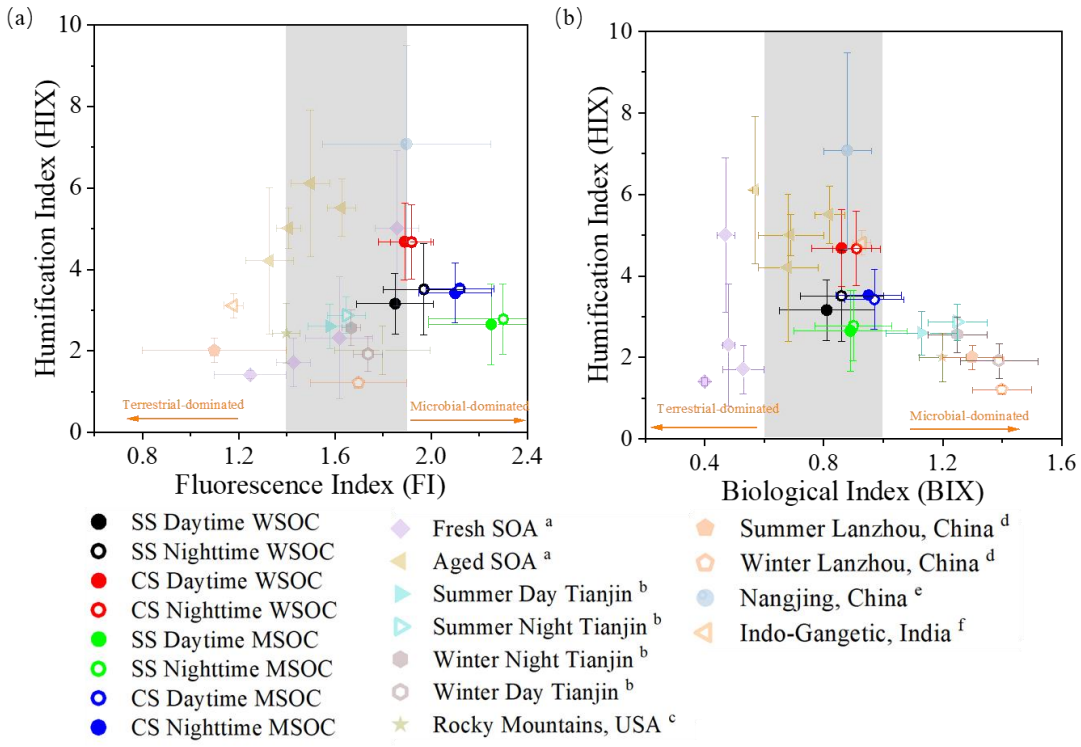

Figure 7. Distribution of the fluorescent indices of measured data in this study and a few other studies ([a] Lee et al. (2013), [b] Deng et al. (2022), [c] Xie et al. (2016), [d] Qin et al. (2018), [e] Xie et al. (2016), [f] Dey et al. (2021)): (a) Humidication index (HIX) versus fluorescenc index (FI), and (b) HIX versus biological index (BIX). The shaded areas marked 0.6 ~ 1 of BIX (Huguet et al., 2009) and 1.6 ~ 1.9 of FI (Mcknight et al., 2001).

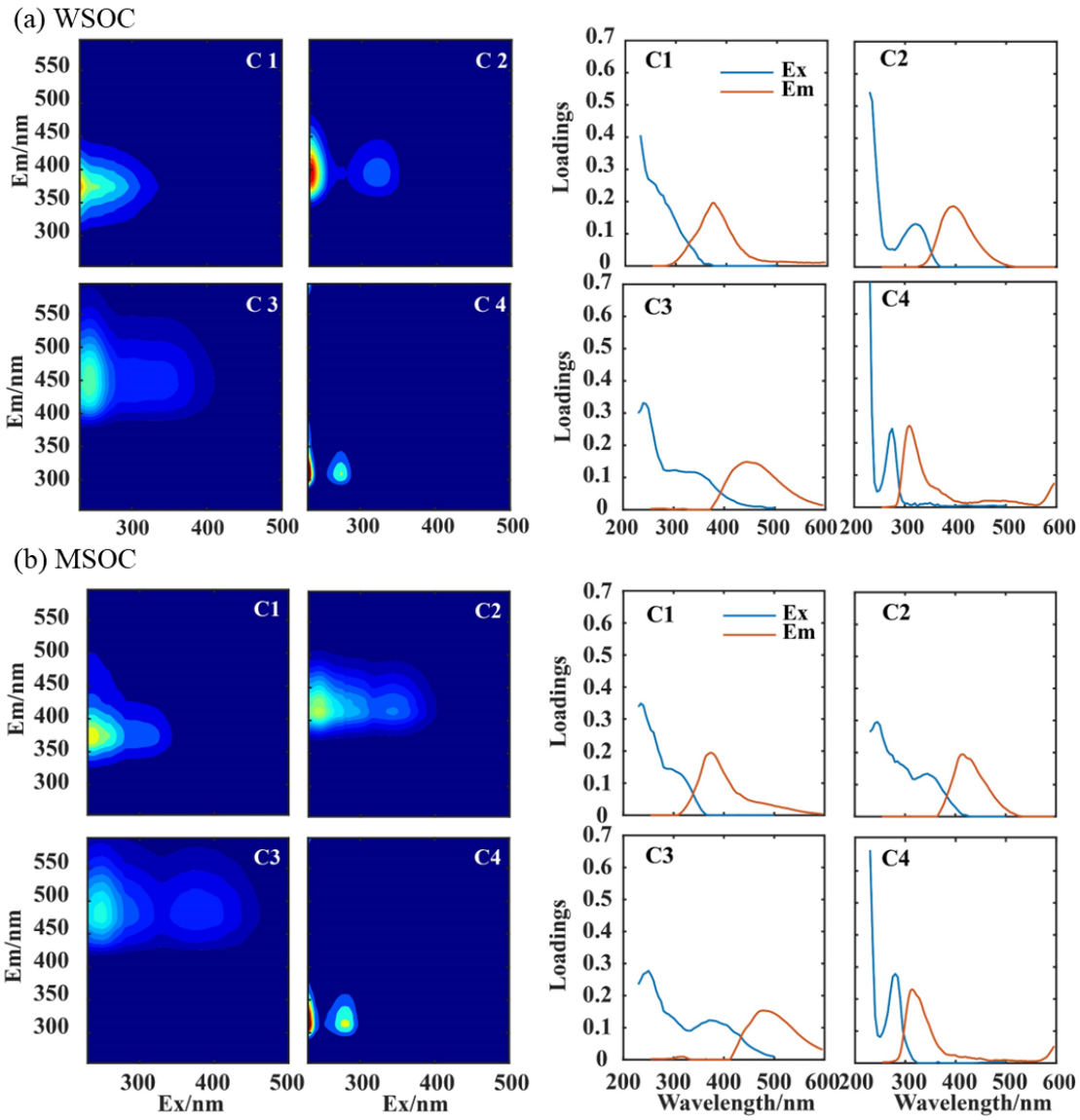

Figure 8. Four fluorescence components (C1 ~ C4) and the corresponding fluorescent intensities of emission (brown) and excitation (blue) against wavelenghth: (a) WSOC, and (b) MSOC.

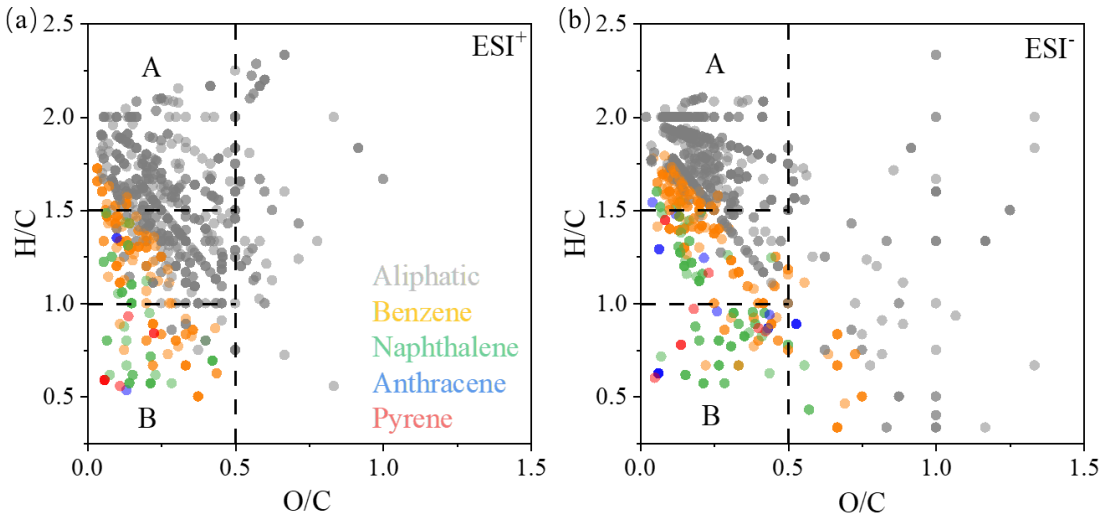

Figure 9. Van Krevelen diagram for CHO compounds detected in (a) ESI^+ and (b) ESI^- mode. The markers with different colors represent aliphatic compounds (Xc < 2.50), aromatic benzene ring structures (2.50 ≤ Xc <2.71), naphthalene ring structures (2.71 ≤ Xc <2.80), anthracene ring structures (2.80 ≤ Xc <2.83), and pyrene ring structures (2.83 ≤ Xc <2 .92), respectively (Mao et al., 2022).

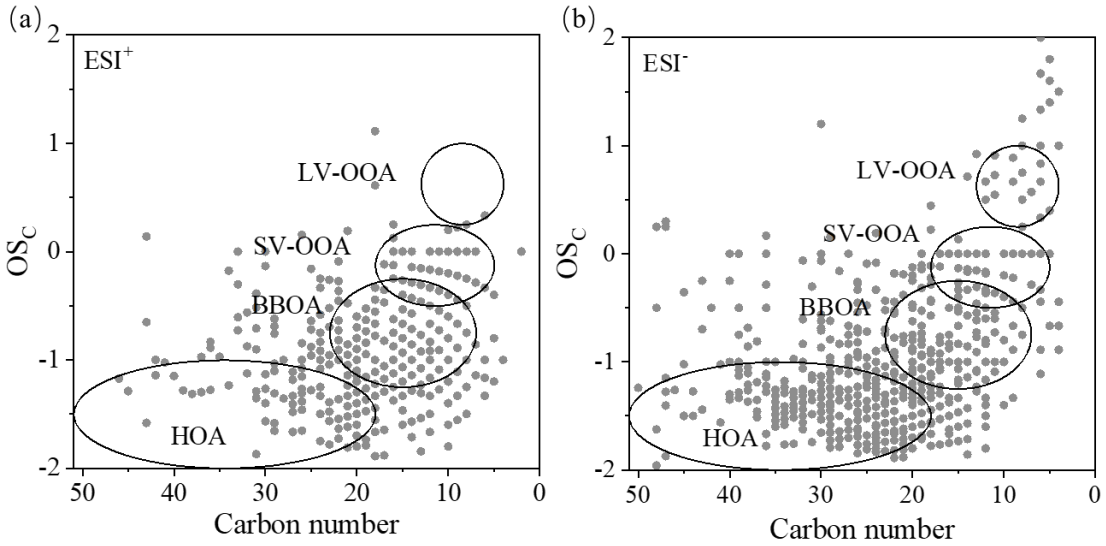

Figure 10. Scatter plots of carbon oxidation state (OSc) versus carbon number for CHO compounds: (a) ESI^+ mode, and (b) ESI^- mode. The circled areas represent those from fossil fuel combustion hydrocarbon-like OA (HOA), biomass burning OA (BBOA), semi-volatile oxygenated OA (SV-OOA) and low-volatility oxygenated OA (LV-OOA)(Kroll et al., 2011).

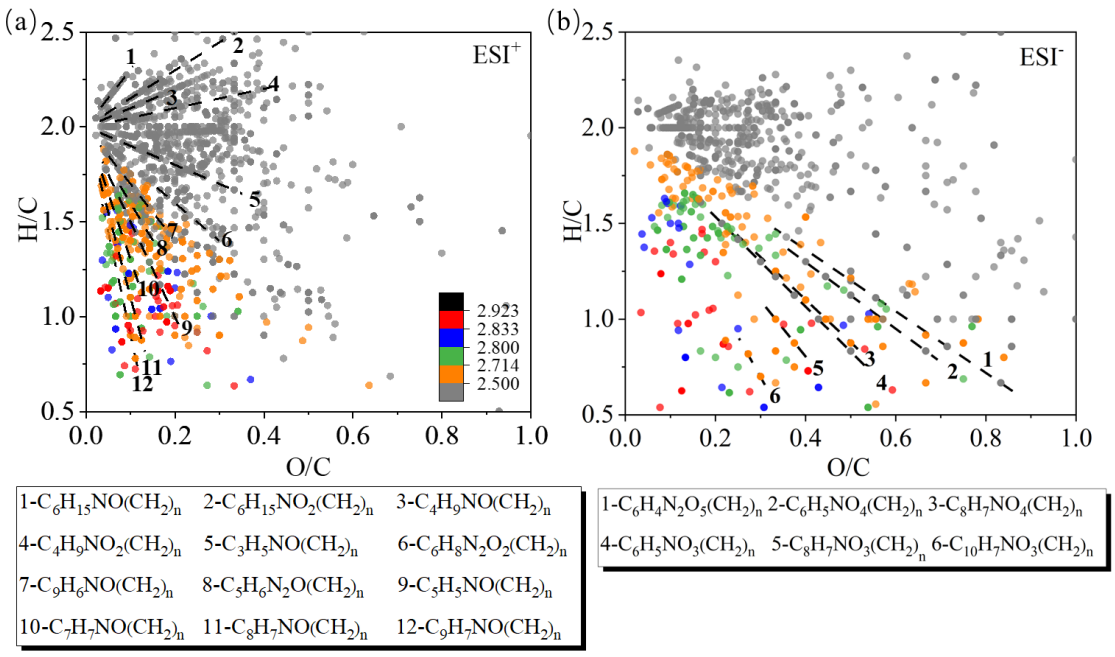

Figure 11. Van Krevelen diagram for CHON compounds detected in both ESI^+ and ESI^- mode. The data are also colored by Xc values (See caption of Fig. 9), and the different dash lines represent different series of compounds.

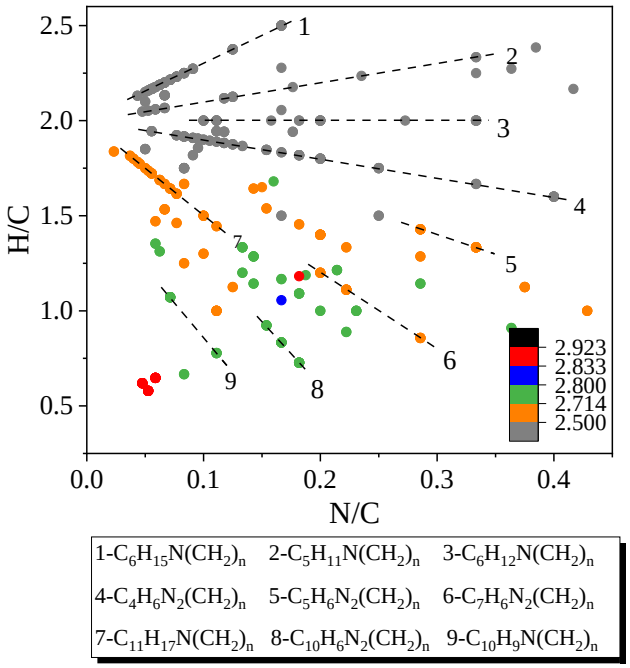

Figure 12. Van Krevelen diagram of the CHN compounds in ESI^+ mode. The data are also colored by Xc values (See caption of Fig. 9), and the different dash lines represent different series of compounds.

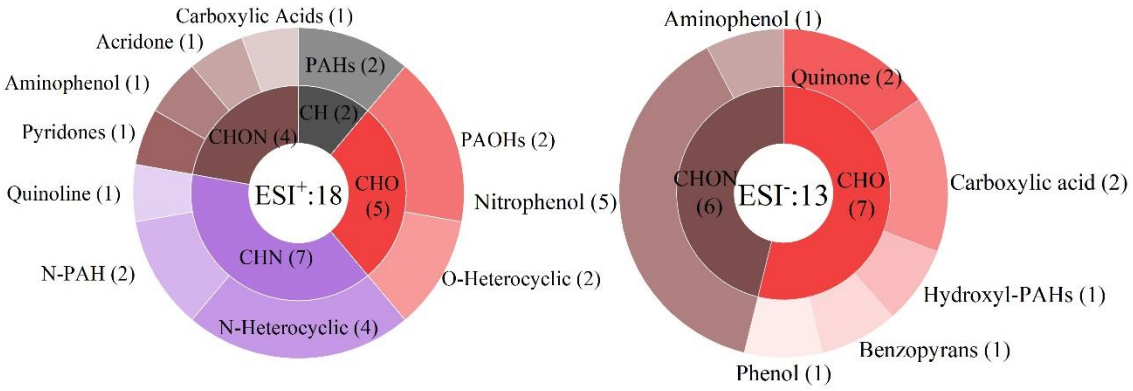

1645

1646 Figure 13. Distributions of the machine learning identified key light absorbing organic

1647 compounds (details in Table S2 in the supplement)

1648